

Understanding the Mechanism and Importance of Brown Carbon Bleaching Across the Visible Spectrum in Biomass Burning Plumes from the WE-CAN Campaign

Yingjie Shen¹, Rudra P. Pokhrel^{1,*}, Amy P. Sullivan², Ezra J. T. Levin^{2,*}, Lauren A. Garofalo³, Delphine K. Farmer³, Wade Permar⁴, Lu Hu⁴, Darin W. Toohey⁵, Teresa Campos⁶, Emily V. Fischer², Shane M. Murphy¹

¹Department of Atmospheric Science, University of Wyoming, Laramie, WY 82071, USA.

²Department of Atmospheric Science, Colorado State University, Fort Collins, CO 80523, USA

³Department of Chemistry, Colorado State University, Fort Collins, CO 80523, USA

⁴Department of Chemistry and Biochemistry, University of Montana, Missoula, MT 59812, USA.

⁵Department of Atmospheric and Oceanic Sciences, University of Colorado Boulder, Boulder, CO 80309, USA

⁶National Center for Atmospheric Research, Atmospheric Chemistry Division, Boulder, CO 80301, USA

*now at Air Pollution Control Division, Colorado Department of Public Health and Environment, Denver, CO 80246, USA

Corresponding author: Shane M. Murphy (shane.murphy@uwyo.edu)

Abstract. Aerosol absorption of visible light has an important impact on global radiative forcing. Wildfires are one of the major sources of light-absorbing aerosol, but there remains significant uncertainty about the magnitude, wavelength dependence, and bleaching of absorption from biomass burning aerosol. We collected and analyzed data from 21 Western United States wildfire smoke plumes during the 2018 WE-CAN airborne measurement campaign to determine the contribution of black carbon (BC), brown carbon (BrC), and lensing to the aerosol mass absorption cross-section (MAC). Comparison to commonly used parameterizations and modeling studies suggest model overestimation of absorption is likely due to incorrect BrC refractive indices. Modelers (Wang et al. 2018; Carter et al. 2021) invoke a bleaching process that decreases the MAC of organic aerosol (OA) to offset the overestimation of absorption in models. However, no evidence of decreasing MAC is observed in individual WE-CAN fire plumes or in aged plumes from multiple fires. A decrease in OA mass and water-soluble organic carbon (WSOC), both normalized by CO to correct for dilution, is observed with increasing oxygen to carbon (O:C) ratio and decreasing gas-phase toluene:benzene ratio, when data from all fires is combined and in half of individual fire plumes. This results in a strong decrease in total absorption at 405 nm and slight decrease at 660 nm with these chemical markers. These results demonstrate that changes in absorption with chemical markers of plume age are the result of decreasing OA rather than changes in the MAC of the organic material itself. While decreasing MAC or OA mass with aging could both be called bleaching, and can both correct overestimation of absorption in models, it's important to distinguish these two effects because decreasing OA mass will also decrease scattering, which will cause a significantly different net radiative effect. We also find that an average of 54% of non-BC absorption (23% total absorption) at 660 nm is from water-soluble BrC, confirming that BrC absorption is important across the visible spectrum. Quantification of significant BrC at red wavelengths and the observation of bleaching being caused by changes in OA with O:C and toluene:benzene markers of plume age provide important improvements to our understanding of BrC and critical constraints on aerosol absorption in regional and global climate models.

38 **1 Introduction**

39 Atmospheric aerosol impact the climate system by directly scattering and absorbing solar radiation, by
40 indirectly changing cloud properties, and through deposition that changes the surface albedo (McConnell et al., 2007;
41 Sarangi et al., 2020). Biomass burning injects a large amount of primary organic aerosol (POA), secondary organic
42 aerosol (SOA) and black carbon (BC) into the atmosphere every year. BC is somewhat poorly defined, but is generally
43 considered to be insoluble and refractory and includes a variety of materials such as char, biochar, charcoal, elemental
44 carbon (EC), and soot (Wei et al., 2013). Although it only represents a small fraction of aerosol mass, BC has a
45 significant impact on the global energy budget due to its ability to strongly absorb solar radiation at all visible
46 wavelengths. While still important, positive radiative forcing of BC is lower in IPCC AR6 (2022) than in IPCC AR5
47 (2013). Bond et al. (2013) estimated the direct radiative forcing for BC from 1750 to 2005 at the top of the atmosphere
48 (TOA) to be $+0.71 \text{ W m}^{-2}$, with an uncertainty of 90% while the latest IPCC AR6 (2022) estimates effective radiative
49 forcing for BC from 1750 to 2019 to be $+0.11 (-0.2 \sim +0.42) \text{ W m}^{-2}$. It is important to note that AR5 reported direct
50 radiative forcing while AR6 reports effective radiative forcing. While BC is emitted from nearly all combustion
51 processes, the largest global source of BC is thought to be biomass burning (Bond et al., 2013). Organic aerosol (OA)
52 also absorbs visible light, but its absorption strongly depends on the wavelength of light (Kirchstetter and Novakov,
53 2004). Non-BC light absorbing organic compounds are often called brown carbon (BrC) and they are usually co-
54 emitted with BC or formed by secondary chemistry in biomass burning plumes (Andreae and Gelencsér, 2006). Unlike
55 BC, which absorbs light from the UV to the IR, BrC absorption sharply increases in the UV and shorter visible portions
56 of the spectrum and has been historically considered to be almost transparent near the red wavelengths (Andreae and
57 Gelencsér, 2006; Bahadur et al., 2012; Liu et al., 2020). The global-mean TOA direct radiative forcing from BrC also
58 shows a large uncertainty, with estimates ranging from $+0.03 \text{ W m}^{-2}$ to $+0.57 \text{ W m}^{-2}$ (Saleh, 2020). Wildfires in the
59 Western U.S. have increased in recent decades (Westerling et al., 2006; Burke et al., 2021), and will continue
60 increasing according to model predictions (Yue et al., 2013; Hurteau et al., 2014; Ford et al., 2018; Neumann et al.,
61 2021). Therefore, quantitative studies of the radiative effects caused by BC and BrC emitted from wildfires are crucial
62 for a better understanding of future climate and essential to improve climate models.

63 The large uncertainty in the radiative forcing from BC is caused both by uncertainties in emissions and by
64 uncertainty in properties that affect its optics, such as size distribution, morphology, refractive index, and mixing state
65 (Bond et al., 2006; Kleinman et al., 2020; Brown et al., 2021). For wildfires, most of the aerosol mass is organic
66 (Garofalo et al., 2019). When BC is internally mixed with OA, the BC is coated by other absorbing or non-absorbing
67 materials that cause more photons to interact with the BC core, and therefore enhance the absorption of the BC core.
68 This process is often called the lensing effect even though geometric lensing is not actually happening at these sizes
69 (Fuller et al., 1999). The absorption enhancement caused by the lensing effect is defined as the ratio of the absorption
70 cross-section of a coated BC particle to that of an equivalent uncoated BC particle (Lack and Cappa, 2010). Laboratory
71 experiments have shown a strong absorption enhancement of BC by a factor of two or more (Schnaiter et al., 2003;
72 Schnaiter et al., 2005; Bond and Bergstrom, 2006; Bond et al., 2006; Peng et al., 2016). Observations of absorption
73 enhancement from ambient BC vary widely in field studies due to variations in coating thickness, coating material,
74 source type, or methodological differences, but it is often much lower than laboratory values (Liu et al., 2015, 2017;

75 Cappa et al., 2012, 2019; Healy et al., 2015; Krasowsky et al., 2016). Cappa et al. (2019) summarized absorption
76 enhancements observed at the red end of the visible spectrum from 10 studies including ambient measurements, source
77 sampling, and lab experiments. The absorption enhancement reported by those measurements ranged from 1.1 to 2.8.

78 The mass absorption cross section of BC (MAC_{BC}) is a different way to describe the absorbing ability of BC
79 containing particles versus absorption enhancement. By describing the absorption per unit mass of BC, MAC_{BC} can
80 be a fundamental input in climate models to convert mass concentration into absorption coefficients (Cho et al., 2019).
81 MAC_{BC} is the particulate absorption divided by the mass of the pure BC at the same wavelength. In this way, the
82 calculated MAC_{BC} will include absorption of the BC core along with the absorption and absorption enhancement
83 caused by the coating material. Unfortunately, the MAC of the overall BC particle, MAC_{BC} , in the ambient atmosphere
84 continues to be poorly understood due to a lack of field measurements and limitations of filter-based instruments to
85 measure this parameter. Processes that occur during atmospheric aging of BC also introduce uncertainties in its
86 absorption. Bond and Bergstrom (2006) suggested a MAC_{BC} of $7.5 \pm 1.2 \text{ m}^2 \text{ g}^{-1}$ at 550 nm for fresh BC. Subramanian
87 et al. (2010) reported a MAC_{BC} of $10.9 \pm 2.1 \text{ m}^2 \text{ g}^{-1}$ at 660 nm and $13.1 \text{ m}^2 \text{ g}^{-1}$ at 550 nm over Mexico City when using
88 a single particle soot photometer (SP2) and the filter-based particle soot absorption photometer (PSAP) instrument
89 during airborne measurements. Krasowsky et al. (2016) reported a MAC_{BC} enhancement of 1.03 ± 0.05 due to the
90 coatings on BC. Zhang et al. (2017) found a MAC_{BC} with a mean of $10 \text{ m}^2 \text{ g}^{-1}$ and a standard deviation of $4 \text{ m}^2 \text{ g}^{-1}$ at
91 660 nm by using both SP2 and PSAP measurements. Cho et al. (2019) summarized MAC_{BC} estimated from more than
92 10 studies in East and South Asia in both ambient conditions and laboratory experiments, and the values ranged from
93 4.6 to $11.3 \text{ m}^2 \text{ g}^{-1}$.

94 The limitations of current measurement techniques bring major uncertainty into quantifying BrC absorption,
95 because BrC is usually co-emitted with BC which makes it challenging to measure BrC absorption independently.
96 BrC absorption can be directly measured through the solvent-extraction method (Peltier et al., 2007; Zeng et al., 2021;
97 Sullivan et al., 2022) or a thermodenuder (Cappa et al., 2012; Liu et al., 2015; Pokhrel et al., 2017). However, the
98 solvent-extraction method will miss BrC that's insoluble in water or organic solvents, and thermal denuders miss BrC
99 that is not volatile at the denuder temperature. BrC absorption can also be calculated from multi-wavelength total
100 absorption measurements, but this approach must assume the absorption Ångström exponent (AAE) for BC and
101 assumes that BrC does not absorb at longer wavelengths, adding significant uncertainty.

102 To improve understanding of the evolution of light-absorbing aerosol from biomass burning, smoke from 21
103 wildfires in the Western United States were measured near their sources and downwind onboard the NSF/NCAR C-
104 130 aircraft during the Western Wildfire Experiment for Cloud Chemistry, Aerosol Absorption and Nitrogen (WE-
105 CAN) campaign. This campaign represented an airborne attempt to fully characterize Western U.S. wildfires from
106 several different fuel types, locations, and fire stages (flaming vs. smoldering). This paper presents novel observations
107 about the absorbing properties of the aerosol and compares these observations to modeling studies conducted with the
108 WE-CAN data and to results from the Fire Influence on Regional to Global Environment – Air Quality (FIREX) study
109 conducted in 2019 (Zeng et al., 2021).

110 **2 Experimental Method**

111 This work relies on measurements made during the WE-CAN field campaign, which sampled smoke emitted
112 by wildfires across the Western U.S. using the NSF/NCAR C-130 research aircraft. The goal of the campaign was to
113 make detailed observations of the physical, chemical, and optical evolution of aerosol in western wildfire smoke and
114 its impact on climate, air quality, weather, and nutrient cycles. The WE-CAN field campaign consisted of 19 research
115 flights that took place from Jul. 24 – Sep. 13, 2018. Data from 13 flights where all required instrumentation was
116 available were analyzed in this study. The flight path and dominant wildfire for each of these flights are shown in Fig.
117 1. The fire locations, fuel types for each fire during WE-CAN were characterized and summarized by Lindaas et al.
118 (2021).

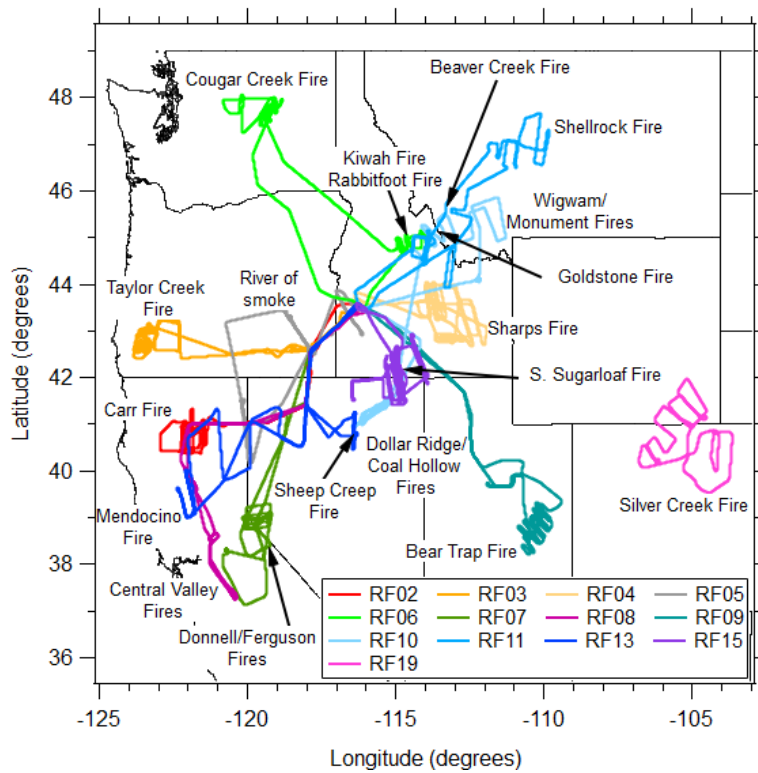


Figure 1: Flight paths and the sampled wildfires for the WE-CAN flights analyzed in this paper.

119 **2.1 Instrumentation**

120 The following instruments are a subset of those flown during the WE-CAN campaign and are utilized in this
121 work. The full WE-CAN dataset is archived at https://data.eol.ucar.edu/master_lists/generated/we-can. All aerosol
122 instruments utilized in this paper, except the PILS, pulled air from the same Solid Diffuser Inlet (SDI) inlet. The PILS
123 sampled from a Submicron Aerosol Inlet (SMAI) (Craig et al., 2013a, 2013b, 2014; Moharreri et al., 2014). All the
124 measurements were converted to standard temperature and pressure (STP, 1 atm, 0°C) based on the measured
125 temperature and pressure (Eq. 1) before data were uploaded.

$$Variables_{STP} = Variables_{measured} \cdot \frac{Pressure_{STP}}{Pressure_{measured}} \cdot \frac{Temperature_{measured}}{Temperature_{STP}} \quad (Eq. 1)$$

2.1.1 Photoacoustic Absorption Spectrometer (PAS)

Aerosol absorption coefficients were measured with the multi-wavelength PAS built by the University of Wyoming (Foster et al., 2019), based on the design of Lack et al. (2012b). A PAS can directly measure the absorption coefficient of dry aerosol. The PAS represents the only way to directly measure aerosol absorption other than a photothermal interferometer (PTI, Sedlacek, 2007), which measures the change in the refractive index of the air near particles caused by heating from absorption. Briefly, when modulated laser light (at the resonant frequency of the cell) is absorbed by the aerosol it heats the surrounding air inducing pressure waves that are amplified by the cavity then detected by two microphones (Lack et al., 2006; Foster et al., 2019). The PAS used here has four cells that measure the aerosol absorption coefficient from dry air at 405 nm and 660 nm and thermally denuded air at 405 nm and 660 nm. The denuder was set to 300°C, with the goal of evaporating volatile organic aerosol which might have a potential impact on light absorption. However, absorption from the denuded channels was not used in this study, because the absorption enhancement calculated using the thermodenuder approach was much smaller than the approach taking the ratio of MAC_{BC} to $MAC_{BC-core}$, and we believe the discrepancy is due to the presence of significant residual organic material after denuding. Two NO_x denuders coated with potassium hydroxide, guaiacol and methanol were installed on the PAS in front of the inlet to remove the absorption from gas-phase NO_2 (Williams and Grosjean 1990). No evidence of NO_2 absorption (which would cause baseline shifts) was observed during filter measurements that are acquired every few minutes. A 3 LPM $PM_{2.5}$ cyclone (URG-2000-30ED) was used on the PAS in front of the inlet to provide a $PM_{1.0}$ cut under a total flow rate of 5.7 LPM. In addition, a Nafion drier (Purma Pure PD-100T-24MPS) with 100 tubes was installed on the inlet system to dry sample to a relative humidity below 30%. The particle loss (< 3%) in the drier was corrected during post-processing. The uncertainty in the absorption coefficient measured by the PAS mainly comes from the calibration technique, in which the highly absorbing substance Regal Black and the CAPS PM_{SSA} were utilized (Foster et al., 2019). The PAS was routinely calibrated (after each flight or every other day if there was a flight everyday) during WE-CAN with an accuracy of +/- 10%.

The PAS microphone shows a pressure-dependent response to pressure. To account for this behavior, we performed pressure-dependent calibration of the PAS where the instrument pressure (both PAS and CAPS PM_{SSA}) was dropped stepwise by ~50 torr from ambient to ~300 torr (typical minimum pressure level during WE-CAN). A calibration was performed at each pressure step and the calibration constants were fitted with pressure to get a change in calibration at a desired pressure. Pressure-dependent calibrations were repeated pre and post-campaign to capture variability.

2.1.2 Cavity-Attenuated Phase Shift Spectrometer (CAPS PM_{SSA})

After pulling through the NO_x denuder, the $PM_{1.0}$ cyclone, and the Nafion drier in front of the PAS inlet, the sampled air entered through the Aerodyne CAPS PM_{SSA_450} and CAPS PM_{SSA_660} to measure the aerosol scattering and extinction coefficients at 450 nm and 660 nm, respectively. CAPS PM_{SSA} instruments measure extinction by utilizing the cavity attenuated phase shift spectroscopy and measure scattering with an integrating sphere (Onasch et

161 al., 2015). Ammonium sulfate particles were used to calibrate the scattering channel of the CAPS PM_{SSA} during WE-
162 CAN with an accuracy of +/- 3%.

163 **2.1.3 Particle-into-Liquid Sampler (PILS) systems**

164 BrC absorption and water-soluble organic carbon (WSOC) were measured by a Particle-into-Liquid Sampler
165 (PILS) system (Sullivan et al., 2022). The PILS continuously collects ambient particles into purified water and
166 provides a liquid sample with the aerosol particles dissolved in it for analysis (Orsini et al., 2003). The size-cut for the
167 PILS was provided by a nonrotating microorifice uniform deposit impactor (MOUDI) with a 50% transmission
168 efficiency of 1 μm (aerodynamic diameter) at 1 atmosphere ambient pressure (Marple et al., 1991). The total airflow
169 for the PILS was approximately 15 LPM. Upstream of the PILS was an activated carbon parallel plate denuder
170 (Eatough et al., 1993) to remove organic gases. In addition, a valve was manually closed periodically for 10 min
171 diverting the airflow through a Teflon filter before entering the PILS allowing for background measurements. The
172 liquid sample obtained from the PILS was pushed through a 0.2 μm PTFE liquid filter by a set of syringe pumps to
173 ensure insoluble particles were removed. The flow was then directed through a liquid waveguide capillary cell (LWCC)
174 and Total Organic Carbon (TOC) Analyzer for near real-time measurement of BrC absorption and WSOC,
175 respectively. More details and a schematic illustration can be found in Zeng et al. (2021).

176 For the absorption measurement, a 2.5 m path-length LWCC (World Precision Instruments, Sarasota, FL)
177 was used. A dual deuterium and tungsten halogen light source (DH-mini, Ocean Optics, Largo, FL) and absorption
178 spectrometer (FLAME-T-UV-VIS, Ocean Optics, Largo, FL) were coupled to the LWCC via fiber optic cables.
179 Absorption spectra were recorded using the Oceanview Spectroscopy Software over a range from 200 to 800 nm. The
180 wavelength-dependent absorption was calculated following the method outlined in Hecobian et al. (2010). For this
181 study, a 16 s integrated measurement of absorption with a limit of detection (LOD) of 0.1 Mm^{-1} was obtained (Sullivan
182 et al., 2022).

183 For the WSOC measurement, a Sievers Model M9 Portable TOC Analyzer (Suez Waters Analytical
184 Instruments, Boulder, CO) was used. This analyzer works by converting the organic carbon in the liquid sample to
185 carbon dioxide through chemical oxidation involving ammonium persulfate and ultraviolet light. The carbon dioxide
186 formed was then measured by conductivity. The increase in conductivity observed was proportional to the amount of
187 organic carbon in the liquid sample. The analyzer was run in turbo mode providing a 4 s integrated measurement of
188 WSOC with a LOD of 0.1 $\mu\text{g C/m}^3$ (Sullivan et al., 2022).

189 **2.1.4 Single Particle Soot Photometer (SP2)**

190 Refractory black carbon (rBC) number and mass concentrations were measured with a Single Particle Soot
191 Photometer (SP2; Droplet Measurement Technologies) which uses a continuous, 1064 nm Nd:YAG laser to heat
192 absorbing material, primarily rBC, to its vaporization temperature and measures the resulting incandescence (Schwarz
193 et al., 2006). Similar to the CAPS PM_{SSA}, the sampled air was sent through the NO_x denuder, PM_{1.0} cyclone, and
194 Nafion drier in front of the PAS inlet before it went to the SP2. The SP2 was calibrated with PSL and size-selected
195 fullerene soot. On the C-130, the SP2 sample line was diluted with HEPA-filtered, pressured ambient air that was

196 passed through a mass flow controller to prevent signal saturation. During post-processing the data was corrected for
197 dilution back to ambient concentrations.

198 **2.1.5 Ultra-High Sensitivity Aerosol Spectrometer (UHSAS)**

199 Particle number concentration was measured by a rack-mounted Ultra-High Sensitivity Aerosol Spectrometer
200 (UHSAS). The flow rate of the rack-mounted UHSAS can be manually lowered by the in-flight operator when the
201 aircraft flew across smoke plumes, so that the UHSAS can stay within its optimum concentration measurement range
202 (Sullivan et al., 2022). The UHSAS was calibrated with ammonium sulfate. The particle mass concentration was
203 calculated by applying these size bins and multiplying by a particle density of 1.4 g cm^{-3} (Sullivan et al., 2022). The
204 volume mean diameter of the particles for all the detected plumes range between $0.18 \text{ }\mu\text{m}$ and $0.34 \text{ }\mu\text{m}$.

205 **2.1.6 Proton-Transfer-Reaction Time-of-Flight Mass Spectrometer (PTR-ToF-MS)**

206 The University of Montana proton-transfer-reaction time-of-flight mass spectrometer (PTR-ToF-MS 4000,
207 Ionicon Analytik) was utilized to report the VOC mixing ratios during WE-CAN (Permar et al., 2021). Only the
208 toluene and benzene mixing ratio derived from the PTR-ToF-MS were used in this work; their overall uncertainty is
209 $< 15\%$. More details of the operation, calibration, and validation on the PTR-ToF-MS during WE-CAN can be found
210 in Permar et al. (2021).

211 **2.1.7 High-Resolution Aerosol Mass Spectrometry (HR-AMS)**

212 Organic aerosol (OA) was detected by the high-resolution aerosol mass spectrometry (HR-AMS; Aerodyne
213 Inc.). The description of the AMS operation during WE-CAN can be found in Garofalo et al. (2019). The atomic
214 oxygen-to-carbon ratios (O:C) and organic mass-to-organic carbon ratio (OM:OC) used in this work were determined
215 via the improved ambient elemental analysis method for the AMS (Canagaratna et al., 2015). Average (integrated)
216 elemental ratios were obtained by averaging (integrating) elemental masses of carbon, hydrogen, and oxygen and
217 recalculating elemental ratios.

218 **2.1.8 Quantum Cascade Laser (QCL) and Picarro Cavity Ring-Down spectrometer (Picarro)**

219 The carbon monoxide (CO) mixing ratio was measured by both an Aerodyne quantum cascade laser
220 instrument (CS-108 miniQCL) and a Picarro cavity ring-down spectrometer (G2401-m WS-CRD) (Garofalo et al.,
221 2019). Because the QCL has better precision than the Picarro instrument, CO measurements from the QCL were
222 preferentially used. However, CO measurements from the Picarro CO data were used for RF10 and RF13, because the
223 CO-QCL was not operated during those two flights. The carbon dioxide (CO_2) mixing ratio was also determined from
224 the Picarro.

225 **2.2 Plume Physical Age**

226 The physical age of the plume was calculated by dividing the distance the plume was sampled from the fire
227 source by the in-plume average wind speed. The average wind speed was measured on the NSF/NCAR C-130 aircraft

228 during each plume pass. The distance was estimated by using the longitude and latitude of the geometric center of the
 229 plume measured on the NSF/NCAR C-130 and the fire location provided by the U.S. Forest Service. The same method
 230 was used by Garofalo et al. (2019), Peng et al. (2020), Lindaas et al. (2021), Permar et al. (2021), and Sullivan et al.
 231 (2022) and are also utilized here for consistency.

232 **2.3 Plume Integration Method**

233 During the WE-CAN campaign, both the SP2 and PILS had significant hysteresis compared to other
 234 instruments. In the SP2 this is because the sampled air was diluted with particle-free ambient air at various ratios to
 235 prevent signal saturation. In the PILS this is because of the retention effect of liquid on the wetted component or within
 236 dead volumes (Zeng et al., 2021). Therefore, it was most accurate to integrate properties across airborne transects of
 237 wildfire plumes to avoid the impact of instrument hysteresis and measurement noise that can dramatically impact
 238 instantaneous ratios. Pseudo-Lagrangian sampling was used during the flights for the WE-CAN campaign, the C-130
 239 aircraft repeatedly crossed the smoke plume from a particular fire by traveling perpendicular to the prevailing winds,
 240 crossing the plume, turning, then crossing the plume again further downwind. In this work, we manually identified
 241 plume edges based on the inflection point when CO concentrations stopped rapidly changing as we entered and exited
 242 the smoke plume. The outside of plume measurement periods had CO mixing ratios from 100 - 300 ppbv. The lowest
 243 10% of each variable from outside plume segments were set to be the background of that variable. If the time between
 244 two consecutive outside plume segments was larger than 20 s and the highest CO mixing ratio was 100 ppbv higher
 245 than the outside plume CO criteria, this segment was chosen as a plume. The start and end point of each plume was
 246 slightly adjusted manually based on the CO mixing ratio to make sure the entire plume was covered. A different start
 247 and end point for the SP2 and PILS was adjusted manually based on the rBC mass concentrations and WSOC,
 248 respectively.

249 **2.4 Absorption Enhancement and Mass Absorption Cross-section**

250 Absorption enhancement (E_{abs}) is the ratio of the absorption of all particles (including BC core and coating
 251 materials) to the absorption of BC alone (Lack and Cappa, 2010). E_{abs} at a specific wavelength ($E_{abs,\lambda}$) was calculated
 252 in this study by Eq. 2:

$$253 \quad E_{abs,\lambda} = \frac{Abs_{Total,\lambda}}{M_{BC} * MAC_{BC,core,\lambda}} \quad (Eq. 2)$$

254 where $Abs_{Total,\lambda}$ is the total absorption coefficient at a wavelength of λ nm measured by the PAS, M_{BC} is the mass
 255 concentration of BC measured by the SP2, and $MAC_{BC,core,\lambda}$ is the MAC of BC alone (without any other coating
 256 material) at λ nm, which is set to be $6.3 \text{ m}^2 \text{ g}^{-1}$ at 660 nm (Bond and Bergstrom, 2006; Subramanian et al., 2010).
 257 MAC_{BC} at λ nm was calculated following Eq. 3:

$$258 \quad MAC_{BC,\lambda} = \frac{Abs_{Total,\lambda}}{M_{BC}} \quad (Eq. 3)$$

259 $MAC_{BC,\lambda}$ is utilized more often in this study than E_{abs} because there is not a widely accepted MAC for BC
 260 emitted from wildfire. MAC of BrC and lensing is calculated at 405 and 660 nm (Eq. 4):

$$MAC_{BrC+lensing,\lambda} = \frac{Abs_{Total,\lambda} - M_{BC} * MAC_{BC_core,\lambda}}{M_{OA}} \quad (Eq. 4)$$

where M_{OA} is the organic mass measured by the AMS. Again, the $MAC_{BC_core,\lambda}$ is set to be 6.3 and 10.2 $m^2 g^{-1}$, respectively, at 660 nm and 405 nm yielding an absorption Ångström exponent (AAE, the negative slope of a logarithmic absorption coefficient against wavelength) of 0.99 for the BC core (Bond and Bergstrom, 2006; Subramanian et al., 2010; Liu, et al., 2015). It should be noted that both BrC and lensing contribute to the $MAC_{BrC+lensing}$, and cannot be separated using this approach. MAC of water-soluble BrC at λ nm ($MAC_{ws_BrC,\lambda}$) is calculated using Eq. 5:

$$MAC_{ws_BrC,\lambda} = \frac{Abs_{ws_BrC,\lambda}}{WSOC * (WSOM:WSOC)} \quad (Eq. 5)$$

where $Abs_{ws_BrC,660}$ is water-soluble light absorption and WSOC is water-soluble organic carbon mass, which are both measured by the PILS system. WSOM:WSOC ratio is set to be 1.6 (Sullivan et al., 2022).

2.5 Fractional non-BC Absorption from BrC

Many previous studies of BrC assume that BrC does not absorb significant amounts of light at long wavelengths (532~705 nm) (Wonaschütz et al., 2009; Lack et al., 2012a; Taylor et al., 2020; Zeng et al., 2021, Zhang et al., 2022). In this study, a PILS system was used to quantify the absorption of light for water-soluble BrC at 660 nm. This absorption is not likely caused by traditional BC, which is insoluble and will be removed by the 0.2 μm filter in the PILS (Peltier et al., 2007; Zeng et al., 2021).

To investigate which contributes more to absorption enhancement at 660 nm, the absorption from BrC or the lensing effect, the fractional non-BC absorption from BrC at 660 nm is calculated by Eq. 6

$$Fractional\ Abs_{BrC} = \frac{Abs_{BrC,660}}{Abs_{Total,660} - M_{BC} * MAC_{BC_core,660}} \quad (Eq. 6)$$

where $Abs_{Total,660}$ is the total absorption coefficient at 660 nm which is measured by the PAS, M_{BC} is the mass concentration of BC which is measured by the SP2, and $MAC_{BC_core,660}$ is the MAC of the BC core at 660 nm which is set to be 6.3 $m^2 g^{-1}$ (Bond and Bergstrom, 2006; Subramanian et al., 2010). $Abs_{BrC,660}$ is the total BrC absorption coefficient at 660 nm, which is calculated from the water-soluble light absorption provided by the PILS, where we convert absorption from water-soluble BrC to total BrC. More specifically, to convert the measured light absorption by water-soluble organics into total BrC absorption in the ambient, it had to be multiplied by two factors. The first factor converts absorption from water-soluble BrC into absorption from total BrC. This factor is obtained by taking the ratio between total particulate organic mass and water-soluble particulate organic mass (OM:WSOM). Water-soluble organic mass is calculated from the PILS WSOC data using a WSOM:WSOC (water-soluble organic mass : water-soluble organic carbon) ratio of 1.6 (Duarte et al., 2015 & 2019). Ambient organic mass is measured by the AMS or calculated from the particle size distributions measured by the UHSAS assuming the particle mass all comes from organic material with a particle density of 1.4 $g\ cm^{-3}$. Both methods are used and compared in this paper. The second factor accounts for the fact that particles absorb more light than the same substance in the bulk liquid phase. Here we use Mie theory (Bohren and Huffman, 1983) to convert absorption from BrC in aqueous solution to the absorption from BrC particles in the ambient (Liu et al., 2013; Zeng et al., 2020). The complex refractive index ($m =$

295 n+ ik) was put into a Mie code (implemented into Igor by Ernie R. Lewis base on Bohren and Huffman, 1983) to
 296 obtain the absorption efficiency (Q), and further used to calculate the absorption coefficient by Eq. 7 (Liu et al., 2013).
 297 The real part of the refractive index (n) is set to be 1.55, and the imaginary part is calculated by using Eq. 8 (Liu et al.,
 298 2013).

$$299 \quad Abs(\lambda, D_p) = \frac{3}{2} \cdot \frac{Q \cdot WSOC}{D_p \cdot \rho} \quad (Eq. 7)$$

$$300 \quad k = \frac{\rho \lambda \cdot H_2O_Abs(\lambda)}{4\pi \cdot WSOC} \quad (Eq. 8)$$

301 where λ is the wavelength, D_p is the diameter of the particle, $Abs(\lambda, D_p)$ is absorption coefficient, Q is absorption
 302 efficiency, particle density (ρ) is set to be 1.4 g cm^{-3} , $WSOC$ is the mass concentration of WSOC ($\mu\text{gC m}^{-3}$) measured
 303 by the PILS, and $H_2O_Abs(\lambda)$ is the water-soluble light absorption coefficient measured by PILS. The plume averaged
 304 particle size distribution was used in the calculation, then the absorption coefficient was calculated for each size bin
 305 of UHSAS to obtain the most accurate Mie factor for each plume.

306 The average OM:WSOM factor based on the UHSAS (UHSAS factor) for all the plumes is 2.36 with a
 307 standard deviation is 1.17. The averaged OM:WSOM based on the AMS (AMS factor) is 1.63 with a standard
 308 deviation of 0.74. The average Mie factor at 660 nm is 1.47 (standard deviation of 0.13), which is close to the factor
 309 of 1.36 found by Zeng et al. (2022) based on FIREX data. The Mie factor at 405 nm based on the WE-CAN data is
 310 also calculated, with an average of 1.83, which is similar to the factor that Zeng et al. (2022) determined at 405 nm
 311 (1.7) based on FIREX and Liu et al. (2013) determined at 450 nm (1.9) based on measurements in Atlanta.

312 Sensitivity tests were done on these factors by choosing reasonable ranges of particle density (1.1 g cm^{-3} , 1.4
 313 g cm^{-3} and 1.7 g cm^{-3}) and WSOM:WSOC ratio (1.5, 1.6 and 1.8) (Duarte et al., 2015 & 2019; Finessi, et al., 2012;
 314 Sun et al., 2011) (Table S1). Particle density only affects the Mie factor and UHSAS factor, while WSOM:WSOC
 315 ratio affects the AMS factor and UHSAS factor. As shown in Table S1, the impact of particle density on the Mie factor
 316 (both at 660 nm and 405 nm) is negligible, WSOM:WSOC is the only component that affects the AMS factor (ranging
 317 from 1.48 to 1.73), while the UHSAS factor is much more sensitive (ranging from 1.65 to 3.06) to both particle density
 318 and WSOM:WSOC. Overall, Table S1 demonstrates that none of the factors other than the UHSAS factor are sensitive
 319 to the exact parameters chosen for the calculation, giving confidence that the results presented are robust.

320 This approach assumes that water insoluble BrC has the same refractive index as water soluble BrC. This
 321 assumption would provide a lower estimation on the BrC contribution to the total absorption because Sullivan et al.
 322 (2022) found that 45% of the BrC absorption at 405 nm in WE-CAN came from water-soluble species, and Zeng et
 323 al. (2022) found that insoluble BrC absorbs more at higher wavelengths than soluble BrC, and methanol-insoluble
 324 BrC chromophores caused 87% of the light absorption at 664 nm.

325 2.6 Absorption of BrC and Water-soluble BrC

326 The bulk absorption coefficient of water-soluble BrC at a specific wavelength ($Abs_{ws_BrC\lambda}$) is measured by
 327 PILS system directly. The bulk absorption coefficient of BrC is calculated from Eq. 9:

$$328 \quad Abs_{BrC+lensing,\lambda} = Abs_{Total,\lambda} - M_{BC} * MAC_{BCcore,\lambda} \quad (Eq. 9)$$

329 where the $Abs_{Total,\lambda}$ is the total absorption coefficient measured by the PAS. MAC of the BC core is set to
330 be 6.3 and 10.2 m² g⁻¹, respectively, at 660 nm and 405 nm. It should be noted that both BrC and lensing contribute to
331 the bulk absorption coefficient, and cannot be separated using this approach.

332 Then the plume integrated absorption and scattering were normalized (x/CO) by taking the ratio of
333 background-subtracted absorption or scattering (Δx) to the background-subtracted CO mixing ratio (ΔCO) (Eq. 10),
334 so that the changing of the normalized properties is not impacted by dilution of the plume with background air.

$$335 \quad x/CO = \frac{\Delta x}{\Delta CO} \quad (Eq. 10)$$

336 **2.7 Modified Combustion Efficiency (MCE)**

337 The variation of burn condition (e.g., flaming vs. smoldering) and fuel type can cause a significant difference
338 in BC emissions and changes in aerosol properties (Akagi et al., 2011; Andreae, 2019). Burn conditions can be
339 estimated with the modified combustion efficiency (MCE), defined as Eq. 11:

$$340 \quad MCE = \frac{\Delta CO_2}{\Delta CO + \Delta CO_2} \quad (Eq. 11)$$

341 where ΔCO_2 and ΔCO are the background-subtracted CO_2 and CO mixing ratio. The background of CO_2 and CO
342 mixing ratio is obtained via the same process described in Section 2.3.

343 **3 Results and Discussion**

344 **3.1 Comparison of WE-CAN MAC_{BrC} to Modeling Studies**

345 It is challenging for climate models to simulate absorption from BrC, especially because it is highly
346 wavelength dependent and may change with chemical age (Liu et al., 2020). Recently the Saleh et al. (2014)
347 parameterization has been implemented in models in an attempt to better parameterize the imaginary part of the BrC
348 refractive index (Wang et al., 2018; Carter et al., 2021). To test how accurately the Saleh parameterization matched
349 WE-CAN data, the BC:OA ratios measured during WE-CAN were input into the Saleh parameterization, which
350 provides an imaginary part for the refractive index of BrC ($k_{BrC,\lambda}$) as a function of the BC:OA ratio. The plume
351 integrated BC:OA ratio for each plume was used in the parameterization, which gave an average k_{BrC} of 0.025, 0.013,
352 0.009, respectively, at 405 nm, 550 nm and 660nm. Mie theory (Bohren and Huffman, 1983) was then used to calculate
353 the MAC for BrC. To do the Mie calculations we assumed a real part of the refractive index of 1.7 for BrC (same as
354 Saleh et al., 2014), used volume mean diameters measured for each plume, and used an organic density of 1.4 g cm⁻³.
355 Figure 2 compares the observed $MAC_{BrC+lensing}$ (Eq. 4) and $MAC_{ws, BrC}$ (Eq. 5) with the value calculated from the Saleh
356 parameterization with inputs from WE-CAN. In both the observations and the parameterization, the MAC_{BrC} decreases
357 as wavelength increases. However, the Saleh parameterization is always significantly larger than the observations.
358 The MAC_{BrC} from the Saleh parameterization, which does not include lensing effects, is a factor of 3.4 and 2.8 larger
359 than the observed $MAC_{BrC+lensing}$ at 405 nm and 660 nm, respectively. The range of BC:OA ratios during WE-CAN
360 (0.007~0.061) is on the very small end of the range (0.005~0.7) used in Saleh's work, and the parameterization failed
361 to capture absorbing aerosol properties for this study. The discrepancy could also be partly because the data Saleh et

362 al. used for their parameterization comes from controlled laboratory burns and not wildfires. It is worth noting that
 363 the Saleh parameterization of MAC_{BrC} is very sensitive to organic aerosol density. If particle density is increased from
 364 1.4 g cm^{-3} to 1.7 g cm^{-3} , the Saleh parameterization median MAC_{BrC} decreases to $1.6 \text{ m}^2 \text{ g}^{-1}$ and $0.24 \text{ m}^2 \text{ g}^{-1}$,
 365 respectively, at 405 nm and 660 nm (a factor of 2.8 and 2.3, respectively, compared to observed MAC_{BrC} at 405 nm
 366 and 660 nm). The fact that the Saleh parameterization overestimates the absorption property of biomass aerosol
 367 especially for fresh emitted aerosols suggests that different parameterizations are needed for the Western U.S.. Carter
 368 et al. (2021) utilized the Saleh parameterization for BrC absorption in the GEOS-Chem model and also found that the
 369 Saleh model overestimated BrC absorption for WE-CAN. It was hypothesized that the overestimation was due to the
 370 lack of a bleaching process for BrC in the model and offset part of the overestimation by bringing in bleaching into
 371 the model.

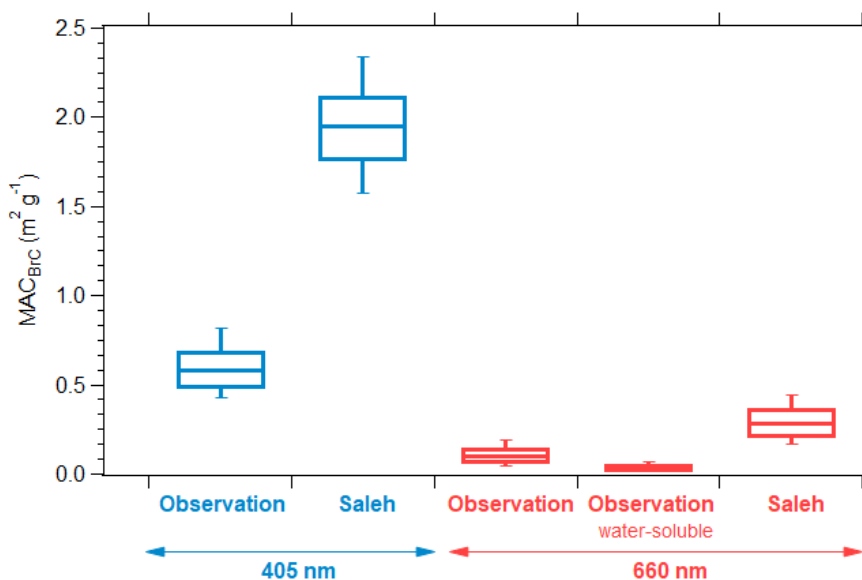


Figure 2: Boxplot summary for observed and parameterized (Saleh) MAC_{BrC} at 405 nm (blue) and 660 nm (red). For each box, the central line represents the median, the top and bottom edges represent the 75th and 25th percentile, and the top and bottom whiskers represent the 90th and 10th percentile of the data.

372 3.2 Investigation of BrC Bleaching at Visible Wavelengths

373 A limited number of field measurements have shown BrC decay with chemical age (Forrister et al., 2015;
 374 Wang et al., 2016). Despite a relatively poor understanding of the mechanism of bleaching or whitening of BrC, this
 375 process has been implemented in numerous model simulations (Brown et al., 2018; Wang et al., 2018; Carter et al.,
 376 2021). The definition of bleaching or whitening is unclear in previous literature, models tend to treat bleaching as the
 377 change of refractive index or decreasing of MAC (Brown et al., 2018; Wang et al., 2018; Carter et al., 2021), while
 378 observations or lab experiments mostly link bleaching to the decrease of absorption coefficient (Forrister et al., 2015;
 379 Palm et al., 2020; Zeng et al., 2022). It is important to distinguish between these two, because the decrease of
 380 absorption coefficient can also be caused by loss of absorbing organic material, which will also change the scattering
 381 coefficient and radiative forcing. Therefore, the MAC of BrC and the absorption coefficient of BrC at visible
 382 wavelengths were calculated and analyzed together with two chemical clocks (O:C and toluene:benzene ratio) and

383 organic mass, to determine whether BrC bleached during the WE-CAN campaign, and whether the bleaching was
384 caused by the less organic mass or the changing of refractive index. Because all large wildfire emissions are a mix of
385 different regions that are burning slightly different fuels at different combustion efficiencies and because models treat
386 regions, not individual fires, we identify relationships in this paper that hold true across all the flight data collected
387 during WE-CAN. These types of broad correlations are much more useful than individual case studies yielding results
388 that only hold true sometimes.

389 3.2.1 Consistency of The Mass Absorption Cross-Section of BrC at 405 nm

390 Palm et al. (2020) combined data from WE-CAN and the Monoterpene and Oxygenated aromatic Oxidation
391 at Night and under LIGHTs (MOONLIGHT) chamber experiment and found that evaporated biomass-burning POA
392 is the dominant source of biomass-burning SOA in wildfire plumes during the first a few hours after emission. They
393 also found that of the SOA formed from oxidation, phenolic compounds contribute $29 \pm 15\%$ of BrC absorption at
394 405 nm. In this section, we analyze the characteristics of BrC at 405 nm to understand the average properties of BrC
395 and to understand the balance of BrC formation versus bleaching during WE-CAN. The MAC of BrC is calculated
396 following Eq. 4 and therefore it includes a contribution from the lensing effect. The MAC of water-soluble BrC is
397 calculated following Eq. 5. Figure 3 shows the MAC of BrC at 405 nm versus the aerosol oxidation level (O:C ratio),
398 while Fig. S2 is a similar plot that uses a simple photochemical clock, the gas-phase toluene:benzene ratio. The O:C
399 ratio characterizes the oxidation state of OA and typically increases with photochemical age (Aiken et al., 2008), while
400 the toluene:benzene ratio decreases with photochemical processing time since toluene is more reactive than benzene
401 (Gouw et al., 2005). Both markers are two commonly used markers to indicate the chemical age of smoke, and they
402 correlated well with each other during WE-CAN (Fig. S1).

403 The $MAC_{BrC+lensing_405}$, varies from $0.08 \text{ m}^2 \text{ g}^{-1}$ to $1.6 \text{ m}^2 \text{ g}^{-1}$ with a mean value of $0.59 \text{ m}^2 \text{ g}^{-1}$ and a standard
404 deviation of 0.19. The largest values are from RF05, the flight through California, Oregon, and Idaho, where aged
405 smoke from different fires was mixed. The large $MAC_{BrC+lensing_405}$ occurred when the aircraft left the smoke-filled
406 boundary layer during RF05. If we exclude $MAC_{BrC+lensing_405}$ from RF05, the values range from $0.08 \text{ m}^2 \text{ g}^{-1}$ to 1.09
407 $\text{m}^2 \text{ g}^{-1}$, but still have a mean value of $0.59 \text{ m}^2 \text{ g}^{-1}$ and a standard deviation of 0.15. Again, we note that this value
408 includes the contribution of lensing. Despite this, our results lie in the same range as those measured without the
409 contribution of lensing of $0.31 \pm 0.09 \text{ m}^2 \text{ g}^{-1}$ measured in CLARIFY-2017 (Taylor, 2020), $0.13\text{-}2.0 \text{ m}^2 \text{ g}^{-1}$ measured
410 in FIREX-AQ (Zeng et al., 2022), and $0.25\text{-}1.18 \text{ m}^2 \text{ g}^{-1}$ measured in ORACLES (Zhang et al., 2022). Very weak or
411 non-trends are observed versus the chemical markers of aging (Fig. 3). If there is any trend, it is a slight increase in
412 MAC_{ws_BrC405} with O:C ratio with a poor correlation. A similar weak trend is also observed when compared
413 MAC_{ws_BrC405} and $MAC_{BrC+lensing_405}$ with the toluene:benzene ratio (Fig. S2). The flat or slightly increasing trend with
414 increasing oxidation level and decreasing toluene:benzene suggests that the refractive index of BrC is not changing in
415 a consistent way at 405 nm. It is important to remember that most of the trends observed in WE-CAN are caused by
416 emissions from different fires versus variations within a single fire, which tend to be quite small. Only 2 flights shows
417 a clear trend ($R^2 > 0.3$) for both MAC_{ws_BrC405} and $MAC_{BrC+lensing_405}$ with increasing O:C ratio at the same time, and
418 they are RF03 (R^2 of 0.85 and 0.85 with positive slope for MAC_{ws_BrC405} and $MAC_{BrC+lensing_405}$), and RF06 (R^2 of 0.8

419 and 0.49 with negative slope for MAC_{ws_BrC405} and $MAC_{BrC+lensing_405}$), where RF03 only measured a single fire (Taylor
 420 Creek fire).
 421

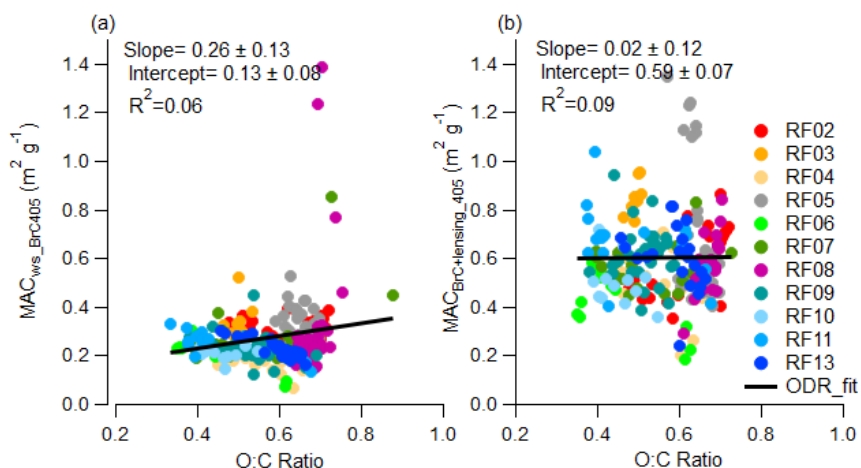


Figure 3: Plume integrated (a) MAC_{ws_BrC405} and (b) $MAC_{BrC+lensing_405}$ variations with the organic aerosol O:C ratio

422 RF05 and RF08 were chosen as case studies, to observe the optical properties of highly aged aerosol to see
 423 if the optical properties of this aerosol were similar to those observed in the near-field plume sampling of individual
 424 fires at the longest chemical or physical age observed, which was roughly 6-24 hours of physical aging. RF08 was a
 425 flight through the Central Valley of California where aged smoke from multiple fires that had settled into the valley
 426 was measured while RF05 was a flight in which smoke from several California fires was observed in California,
 427 Oregon and Idaho roughly 300~600 miles from the fires (flightpaths are shown in Fig. 1). $MAC_{BrC+lensing_405}$, CO
 428 mixing ratio, toluene:benzene ratio, and O:C ratio are displayed in Fig. 4a and 4b. The mixing ratio of CO is relatively
 429 low in these aged dilute smoke plumes vs. the plumes near the sources analyzed earlier. 1-minute averages of
 430 $MAC_{BrC+lensing_405}$ are calculated to reduce noise and 1-minute-averages for toluene:benzene ratio and O:C ratio were
 431 calculated and all the negative values were removed. As shown in Fig. 4, the smallest toluene:benzene ratio is ~0.35
 432 in RF05, and is ~0.16 in RF08, while the largest O:C ratio is ~0.7 in both RF05 and RF08, which indicates these two
 433 cases indeed captured plumes that appear chemically aged to similar extent to the other near-field flights where the
 434 smallest toluene:benzene ratio was 0.33 and the largest O:C ratio was 0.88 in near-fire measurements (Fig. 3 and Fig.
 435 S2).

436 In RF05 (Fig. 4a), the weighted average O:C ratio over the entire flight was 0.64, and the toluene:benzene
 437 ratio averaged 0.45 with a standard deviation of 0.05. $MAC_{BrC+lensing_405}$ varied from $0.36 \text{ m}^2 \text{ g}^{-1}$ to $1.52 \text{ m}^2 \text{ g}^{-1}$ with an
 438 average of $0.66 \text{ m}^2 \text{ g}^{-1}$ and a standard deviation of $0.26 \text{ m}^2 \text{ g}^{-1}$. The plume that was measured in this flight was a
 439 mixture of different fire sources. Despite the much longer transit time and distance, overall these emissions, which
 440 were measured 300 to 600 miles away, have a very similar $MAC_{BrC+lensing_405}$ to that of the near-source flights.

441 The RF08 (Fig. 4b) results are similar to RF05, even though these emissions were smoke of mixed aged from
 442 multiple fire sources in the Central Valley of California. The weighted average O:C ratio was 0.67 over the entire
 443 measurement, and average toluene:benzene ratio was 0.41 with a standard deviation of 0.15. $MAC_{BrC+lensing_405}$

444 averaged $0.59 \text{ m}^2 \text{ g}^{-1}$ with a standard deviation is $0.14 \text{ m}^2 \text{ g}^{-1}$. There are several extreme values that exist in the dataset,
 445 probably because of time-alignment issues caused by variation in the dilution rate of the SP2 which cannot be totally
 446 eliminated from the 1-minute average. In addition, the smoke from RF08 (Fig. 4b) is split into four regions based on
 447 varying observed CO mixing ratios, and integrated $\text{MAC}_{\text{BrC+lensing}_405}$ is calculated for each region (purple star marker).
 448 The regional edges are represented by blue dashed lines. Integrated $\text{MAC}_{\text{BrC+lensing}_405}$ for all of these variable CO
 449 regions is relatively stable with an average value of $0.59 \text{ m}^2 \text{ g}^{-1}$ and a standard deviation of $0.07 \text{ m}^2 \text{ g}^{-1}$.
 450

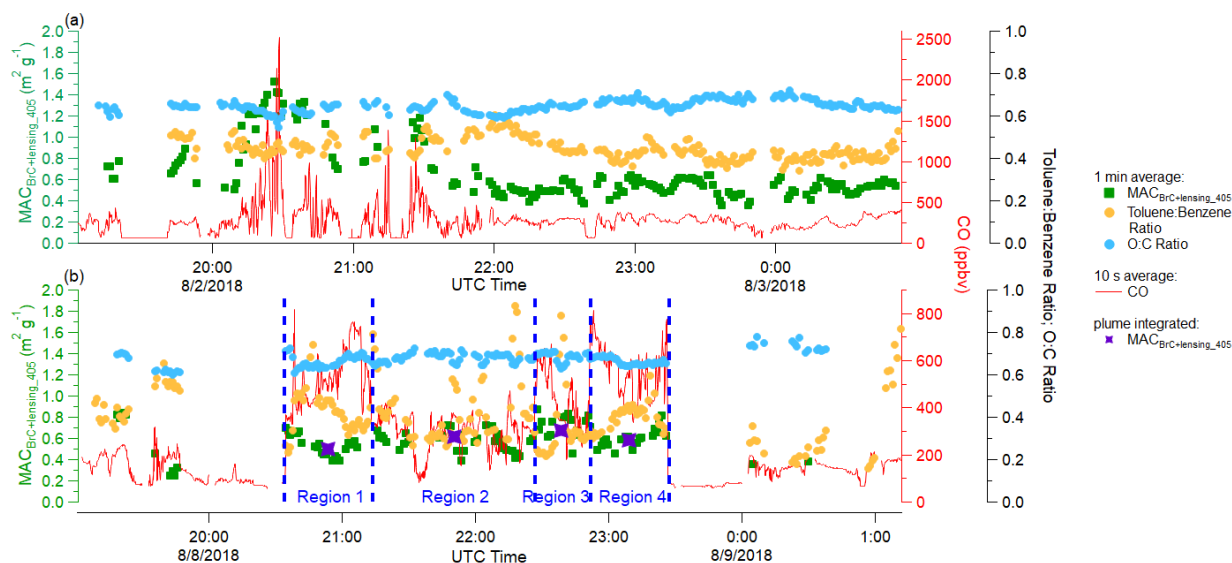


Figure 4: Time series of plume properties during (a) RF05 (measurements far from fire source), and (b) RF08 (Central Valley of California). Different square and round markers indicate 1 min averages of different variables as shown in the legend, and the red solid line represents 10 s averages of the mixing ratio of CO. Purple stars in RF08 indicate region integrated $\text{MAC}_{\text{BrC+lensing}_405}$ (individual regions are separated based on the concentration of CO, and indicated by blue dashed lines).

451 3.2.2 Decrease in Absorption at 405 nm Observed with Markers of Chemical Oxidation

452 Although neither the $\text{MAC}_{\text{BrC+lensing}_405}$ nor $\text{MAC}_{\text{ws}_\text{BrC}405}$ decreases with O:C or Toluene:Benzen, Fig. 5
 453 shows that BrC bleaching is observed in terms of decreased total absorption. Figure 5a and 5c show the behavior of
 454 BrC absorption at 405 nm with markers of the aerosol oxidation level (O:C) and photochemistry (toluene:benzene).
 455 The absorption coefficient of BrC shown in Fig. 5 is calculated by Eq. 9-10, which cannot separate the absorption
 456 caused by the BrC and lensing effect. To confirm that observed trends are not the result of changing lensing, the
 457 absorption coefficient of water-soluble BrC measured by the PILS, which does not include lensing effects, is also
 458 compared in Fig. 6a and 6c. The average water-soluble BrC absorption at 405 nm ($\text{Abs}_{\text{ws}_\text{BrC}405}$, $0.02 \text{ Mm}^{-1} \text{ ppbv}^{-1}$)
 459 is only 20% of the total absorption from BrC plus lensing ($\text{Abs}_{\text{BrC+lensing}_405}$, $0.11 \text{ Mm}^{-1} \text{ ppbv}^{-1}$). However,
 460 $\text{Abs}_{\text{BrC+lensing}_405}$ and $\text{Abs}_{\text{ws}_\text{BrC}405}$ both decrease with increasing O:C ($R^2 = 0.65$ and $R^2 = 0.3$, respectively for
 461 $\text{Abs}_{\text{BrC+lensing}_405}$ and $\text{Abs}_{\text{ws}_\text{BrC}405}$) and decreasing toluene:benzene ratio, which suggest a similar level of
 462 decreasing BrC absorption for all the fires observed in WE-CAN from numerous locations in the western U.S.. This
 463 relationship holds despite differences in fuel type, burn conditions, meteorology, etc. between all of these fires. The

464 observed trends are mostly due to the decreasing of both total OA mass (Fig. 5b and 5d) and WSOC (Fig. 6b and 6d)
465 with the increasing O:C ratio ($R^2 = 0.8$ and $R^2 = 0.4$, respectively for OA and WSOC) and decreasing toluene:benzene
466 ratio ($R^2 = 0.64$ and $R^2 = 0.44$, respectively for OA and WSOC). Overall, the organic aerosol O:C ratio better predicts
467 BrC evolution than toluene:benzene ratio, probably because it is a particle-phase property rather than a gas-phase one.
468 Again, it is important to clarify if BrC “bleaching” is caused by decreasing BrC absorption coefficient or decreasing
469 of BrC refractive index (or MAC). In this study, decreasing MAC_{BrC} is not observed, rather the BrC absorption
470 coefficient decreases significantly with the the simple O:C and Toluene:Benzene chemical clocks due to loss of OA
471 mass. Less OA mass also causes decrease in bulk scattering coefficient (Fig. S3), leading to a very different net
472 radiative effect than reducing MAC_{BrC} .

473 It is important to recall that we aimed to find general trends that hold for all fires in the western U.S., and the
474 above trend is significant when all fires are grouped together, although the trend is, in fact, not robust in each flight
475 and is rather due to variations between the fire plumes rather than variation within a single fire plume. Figure 7 shows
476 the correlation between normalized OA and chemical age for each fire source. It demonstrates that different fires show
477 different relationships and that OA does not always decrease with oxidation level/chemical aging within a single fire
478 (Kiwah fire and Rabbitfoot fire), though increasing O:C ratio does correlate well ($R^2 > 0.3$) with decreasing OA mass
479 in 7 fires (with R^2 of 0.94 for Taylor Creek fire, 0.87 for Carr fire, 0.86 for Beaver Creek fire, 0.8 for Coal Hollow
480 fire, 0.76 for Bear Trap fire, 0.35 for Sharps fire, and 0.31 for Sugarloaf fire). Toluene:benzene ratio didn’t track OA
481 as good as O:C ratio, and decreasing toluene:benzene ratio correlates well ($R^2 > 0.3$) with decreasing OA mass in 3
482 fires (with R^2 of 0.87 for Rabbitfoot fire, 0.85 for Coal Hollow fire, and 0.84 for Bear Trap fire).

483

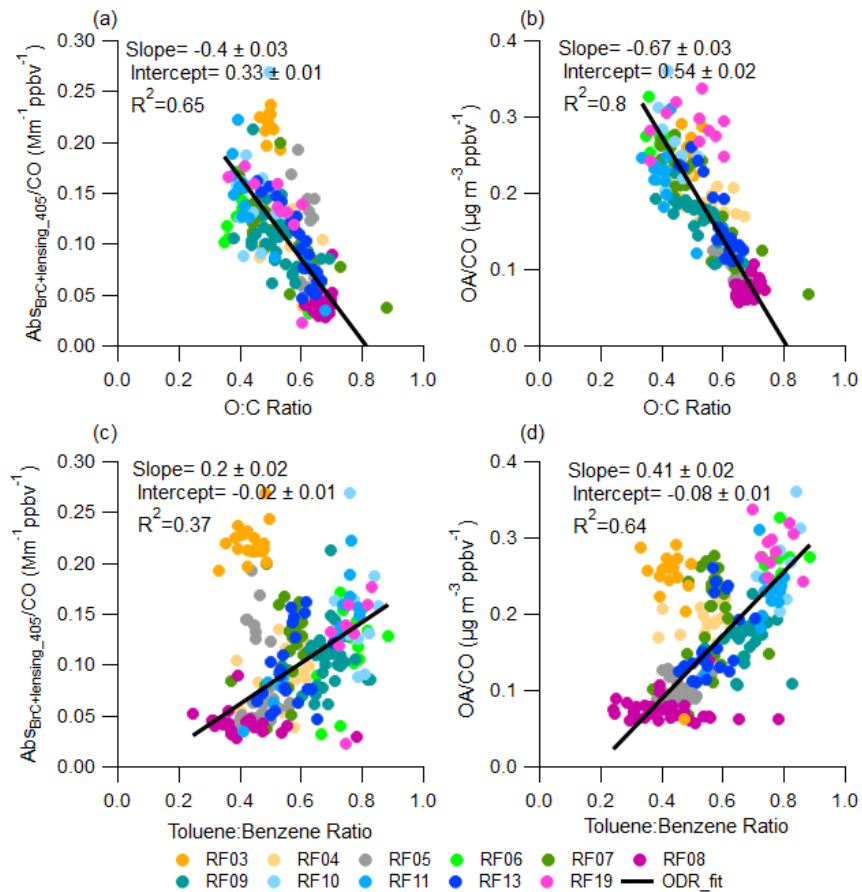


Figure 5: Plume integrated normalized $Abs_{BrC+lensing_405}$, and OA variation with chemical age. Top panels show (a) plume integrated normalized $Abs_{BrC+lensing_405}$, and (b) plume integrated normalized OA variation with O:C ratio. Bottom panels show (c) plume integrated normalized $Abs_{BrC+lensing_405}$, and (d) plume integrated normalized OA variation with toluene:benzene ratio. Data from RF03 was excluded from the ODR fit with toluene:benzene ratio, because RF03 sampled the injection of fresh smoke into the free troposphere, where gas species reacted more rapidly than particles and toluene:benzene ratio failed to keep track of aerosol evolution.

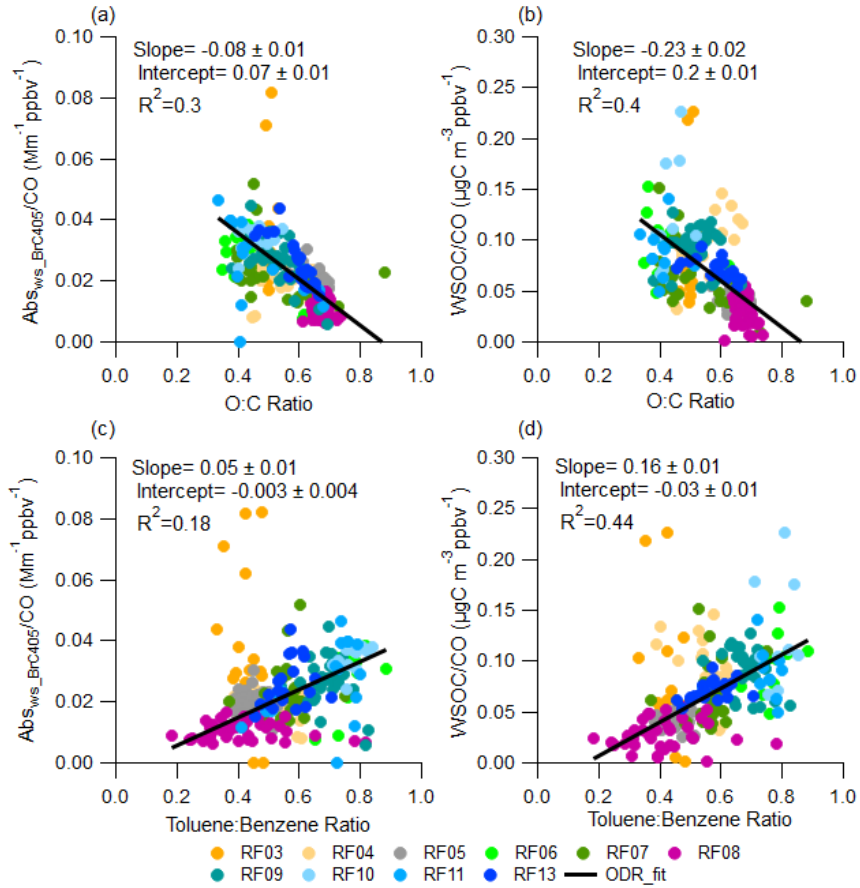


Figure 6: Similar to Fig. 5, but with plume integrated normalized Abs_{ws_BrC405} , from PILS in (a) and (c), and WSOC in (b) and (d)

485

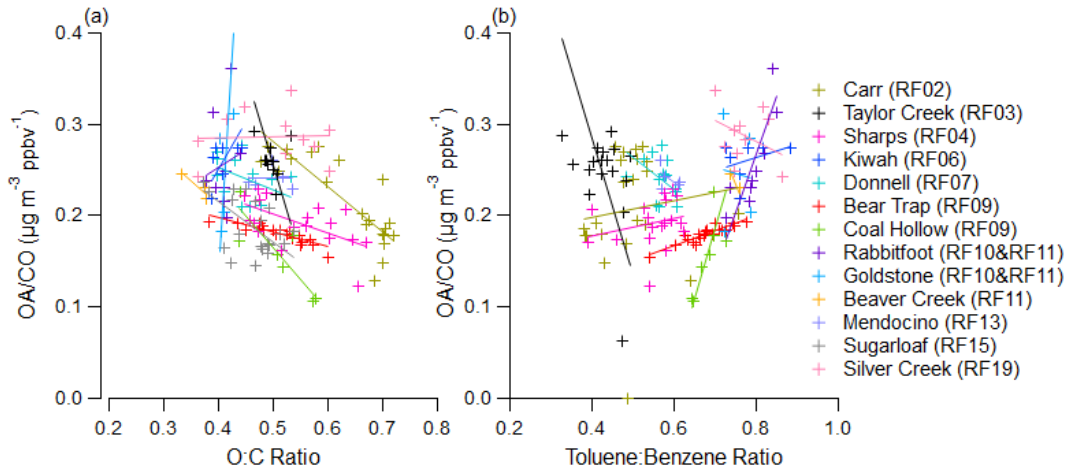


Figure 7: Plume integrated normalized OA variation with (a) O:C ratio and (b) toluene:benzene ratio. Different colors were used to distinguish plumes from different fire sources. Plumes from uncertain fire sources (especially plumes from RF05, RF08) were not included in this plot.

486

487 No trend is observed in CO normalized OA mass with plume physical age (Fig. S4), which is consistent with
488 the result from Garofalo et al. (2019) in that no net OA mass change was observed in individual plumes during WE-
489 CAN when they are characterized by physical age, although more data from additional fires were included in the
490 current work. Plume-integrated CO-normalized OA also shows weak or no trend with altitude and temperature (Fig.
491 S5). However, we note that the smallest OA:CO was captured in the plumes (RF08) that have highest temperature
492 (~305 K), and larger OA:CO tends to be observed in the colder plumes (RF19). More studies are needed to determine
493 how much OA is evaporated in high temperature plumes because the WE-CAN dataset does not capture enough
494 variation of temperature within plumes to make a robust conclusion. No clear trend was found between
495 $MAC_{BrC+lensing_405}$ and physical age or MCE (Fig. S6). Similar behavior was also observed in Western wildfires at 405
496 nm in FIREX-AQ (Zeng et al., 2022). Part of the reason is that for most fires, we only captured the first few hours (<
497 15 h), and MCE do not have a robust capability to predict biomass burning particle properties (McClure et al., 2020).
498 No trend is found between $MAC_{BrC+lensing_405}$ and altitude or temperature (Fig. S7). The trend with BC:OA ratio (Fig.
499 S8) is not as clear as in Saleh et al. (2014), most probably because the range of BC:OA ratios observed during WE-
500 CAN (0.007~0.061) is much smaller than that (0.005~0.7) observed in Saleh's work. Even in their work, the increasing
501 trend is not very clear if one only focuses on the region where the BC:OA ratio is less than 0.03. Also, the Saleh et al.
502 (2014) results were obtained from laboratory burns and not wildfires, which might also cause a discrepancy.

503 3.2.3 Mass Absorption Cross-Section and Optical Properties of BrC at 660 nm

504 BrC is defined as OA that has strong absorption at UV and shorter visible portions of the spectrum and has
505 been historically considered to be almost transparent near the red wavelengths (Andreae and Gelencsér, 2006; Bahadur
506 et al., 2012; Liu et al., 2020). However, during WE-CAN, we were able to quantify Abs_{ws_BrC660} with the PILS
507 instrument. We know that absorption observed in the PILS at 660 nm is not BC because BC is insoluble and will be
508 removed by the 0.2 μ m filter in the instrument. Next, we investigate the behavior of BrC absorption at 660 nm to see
509 if BrC has a similar behavior at the long versus short ends of the visible spectrum.

510 Figure 8 shows the behavior of brown carbon at 660 nm vs. the O:C ratio. Similar to 405 nm, no bleaching
511 in terms of decreased MAC is observed at 660 nm. If there is any trend, it is increasing MAC_{ws_BrC660} and
512 $MAC_{BrC+lensing_660}$ with organic aerosol O:C ratio. Similar trends are observed, though with lower correlation, versus
513 the toluene:benzene ratio (Fig. S9). The mean value of $MAC_{BrC+lensing_660}$ is $0.11 \text{ m}^2 \text{ g}^{-1}$ (with a standard deviation of
514 0.06), which is much larger than the 0.03 average of MAC_{ws_BrC660} , a result we have attributed to the lensing effect,
515 but which could also partially be the result of water-insoluble BrC having a higher MAC than water-soluble BrC.

516 These results for the behavior of MAC_{BrC} at different wavelengths derived using different instruments (PAS
517 and PILS) is further evidence that MAC_{BrC} does not decrease with physical or chemical age in the WE-CAN dataset.
518 At a minimum, the plume integrated results, which represent total optical properties relevant to climate models, do
519 not capture any MAC_{BrC} decay that might be occurring at the edges of the plume.

520

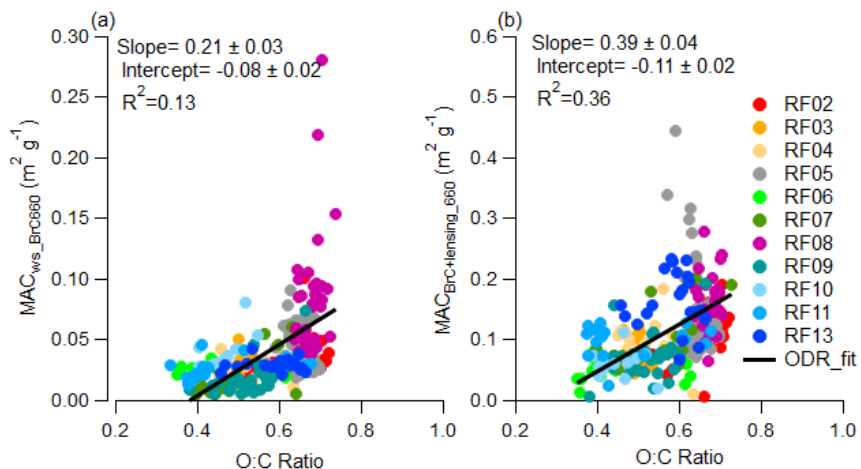


Figure 8: Plume integrated (a) MAC_{ws_BrC660} and (b) $MAC_{BrC+lensing_660}$ variations with O:C ratio

521 Similar to our analysis at 405 nm, RF05 and RF08 are presented as case studies to investigate the behavior
 522 of $MAC_{BrC+lensing_660}$ in aged plumes emitted from different fire sources. Figure 9 is similar to Fig. 4, but with
 523 $MAC_{BrC+lensing_660}$ instead of $MAC_{BrC+lensing_405}$. For the case of RF05 (Fig. 9a) $MAC_{BrC+lensing_660}$ varied from 0.04 m^2
 524 g^{-1} to $0.40 \text{ m}^2 \text{ g}^{-1}$ with an average of $0.15 \text{ m}^2 \text{ g}^{-1}$ and a standard deviation of $0.07 \text{ m}^2 \text{ g}^{-1}$. The $MAC_{BrC+lensing_660}$ tends
 525 to be larger when CO mixing ratio is higher, but does not have a significant correlation with any marker of oxidation
 526 level or photochemistry shown in Fig. 9. For the case of RF08 (Fig. 9b) $MAC_{BrC+lensing_660}$ is more stable than in RF05,
 527 and varied from $0.04 \text{ m}^2 \text{ g}^{-1}$ to $0.37 \text{ m}^2 \text{ g}^{-1}$ with an average of $0.18 \text{ m}^2 \text{ g}^{-1}$ and a standard deviation of $0.06 \text{ m}^2 \text{ g}^{-1}$. The
 528 regional integrated $MAC_{BrC+lensing_660}$ is even more stable with an average value of $0.16 \text{ m}^2 \text{ g}^{-1}$ and a standard deviation
 529 of $0.01 \text{ m}^2 \text{ g}^{-1}$. Similar to the results at 405 nm, we observe that the MAC in these very aged plumes is very similar to
 530 the average MAC observed in the near field.
 531

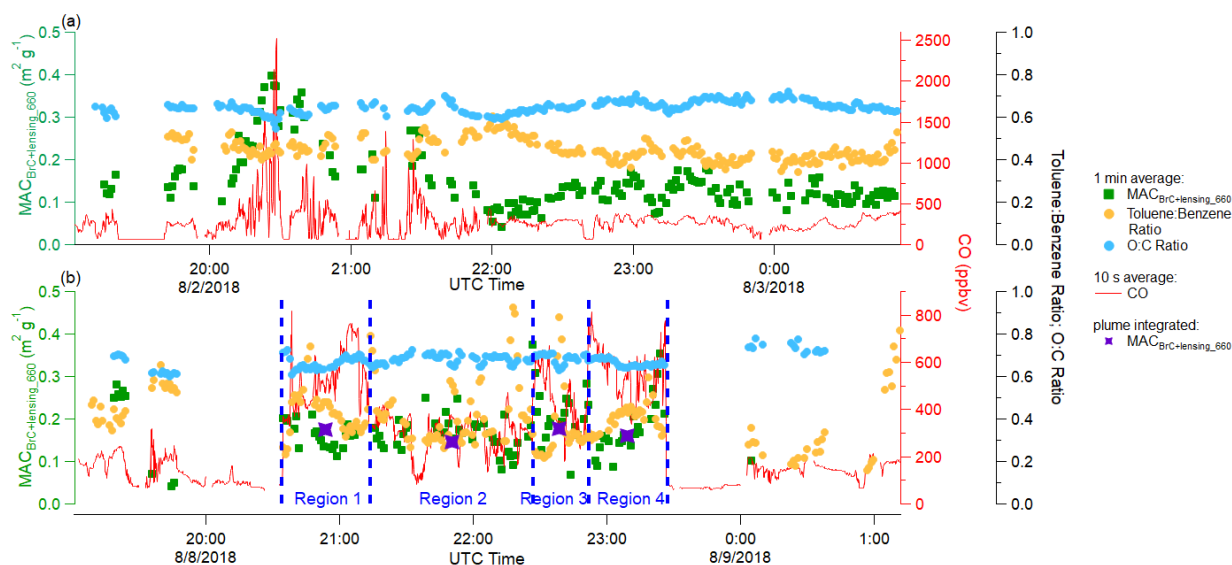


Figure 9: Time series of plume properties during (a) RF05, and (b) RF08(Central Valley of California). Different square and round markers indicate 1 min averages of different variables as shown in the legend, and the red solid line represents 10 s averages of the mixing ratio of CO. Purple stars in RF08 indicate region integrated $MAC_{BrC+lensing_660}$ (individual regions are separated based on the concentration of CO, and indicated by blue dashed lines).

532 Normalized $Abs_{BrC+lensing_660}$ and total scattering coefficient at 660 nm (Fig. S10), as well as normalized
 533 Abs_{ws_BrC660} (Fig. S11) were also investigated to see if they decreased with markers of chemical age similar to the
 534 results seen at 405 nm. However, the correlation between these BrC optical properties with O:C ratio or
 535 toluene:benzene ratio at 660 nm is much weaker and flatter than they are at 405 nm. Perhaps this is because BrC
 536 absorption is very small at 660 nm, and a large uncertainty is brought in from the assumptions required for calculation
 537 of this property and instrumental uncertainties. The average normalized $Abs_{BrC+lensing_660}$ is $0.02 \text{ Mm}^{-1} \text{ ppbv}^{-1}$, which
 538 is 5 times lower than the absorption at 405 nm; while the average normalized Abs_{ws_BrC660} is a order of magnitude
 539 lower than Abs_{ws_BrC405} . The $MAC_{BrC+lensing_660}$ (Fig. S12) shows better correlation with BC:OA ratio than
 540 $MAC_{BrC+lensing_405}$, though the increasing trend is still not as significant as Saleh et al. (2014) due to a much smaller
 541 BC:OA ratio during WE-CAN.

542 3.3 Relative Importance of BrC vs. the Lensing Effect at 660 nm

543 Plume integrated MAC_{BC} at 660 nm (MAC_{BC660}) from the 13 WE-CAN research flights with clear plume
 544 transects of biomass burning plumes are shown in Fig. 10. The MAC_{BC660} discussed in this section is calculated from
 545 Eq. 3, and has contributions from absorption from the BC core, the BrC shell, and the lensing effect. Again, even fire
 546 plumes from individually named fires are usually a mix of many different burning conditions, and it is hard to identify
 547 the exact source in most wildfire smoke measurements, especially for well mixed plumes. Therefore flight-to-flight
 548 data is analyzed because each flight covered a region, and an overall behavior of absorbing aerosol from wildfire can
 549 be provided. MAC_{BC660} varies between different flights with RF03 having the highest average MAC_{BC660} of 12.9 m^2
 550 g^{-1} , and RF10 having the lowest average MAC_{BC660} of $8.6 \text{ m}^2 \text{ g}^{-1}$. Even in highly aged plumes with emissions mixed
 551 from multiple fires (RF05 and RF08), the MAC_{BC660} is similar in magnitude and consistency with an average of 11.3

552 $\pm 1.8 \text{ m}^2 \text{ g}^{-1}$. The average of all plume-integrated $\text{MAC}_{\text{BC660}}$ is $10.9 \text{ m}^2 \text{ g}^{-1}$, with a standard deviation of $2.1 \text{ m}^2 \text{ g}^{-1}$.
 553 This result is similar to some other recent airborne measurements. Subramanian et al. (2010) reported a $\text{MAC}_{\text{BC660}}$ of
 554 $10.9 \pm 2.1 \text{ m}^2 \text{ g}^{-1}$ using a SP2 and PSAP operated during the MILAGRO campaign, which included airborne
 555 measurements of biomass burning over Mexico. Similarly, Zhang et al. (2017) estimated a $\text{MAC}_{\text{BC660}}$ of $10 \text{ m}^2 \text{ g}^{-1}$
 556 utilizing both SP2 and PSAP deployed on the NASA DC-8 research aircraft for the DC3 campaign, which measured
 557 the upper tropospheric BC over the central U.S. Taylor et al. (2020) calculated a $\text{MAC}_{\text{BC655}}$ of $12 \pm 2 \text{ m}^2 \text{ g}^{-1}$ for biomass
 558 burning emissions from Africa over the southeast Atlantic Ocean, using airborne measurements from a SP2 and PAS
 559 in the CLARIFY-2017 campaign.

560 These results are encouragingly similar given the breadth of measurement techniques (PSAP is filter-based
 561 whereas PAS is a direct measurement), geographic regions (Continental U.S. for DC3, Mexico for MILAGRO, African
 562 outflow for CLARIFY) and altitude in the atmosphere (all were airborne campaigns covering a range of altitudes). If
 563 we apply $6.3 \text{ m}^2 \text{ g}^{-1}$ as the MAC of a BC core at 660 nm (Bond and Bergstrom, 2006; Subramanian et al., 2010), then
 564 the average absorption enhancement for the entire WE-CAN campaign is 1.7. This means the absorption of coated BC
 565 is 1.7 times higher than bare BC at 660 nm, which is somewhat close to the factor of ~ 2 reported by laboratory
 566 experiments (Schnaiter et al., 2005; Peng et al., 2016), larger than some field measurements (Cappa et al., 2012&2019;
 567 Healy et al., 2015), but close to 1.85 ± 0.45 measured by Taylor et al. (2020) in African biomass burning plumes. The
 568 similarity to the Taylor et al. (2020) result suggests global similarities in the $\text{MAC}_{\text{BC660}}$ from aerosol emitted from
 569 wildfires.

570

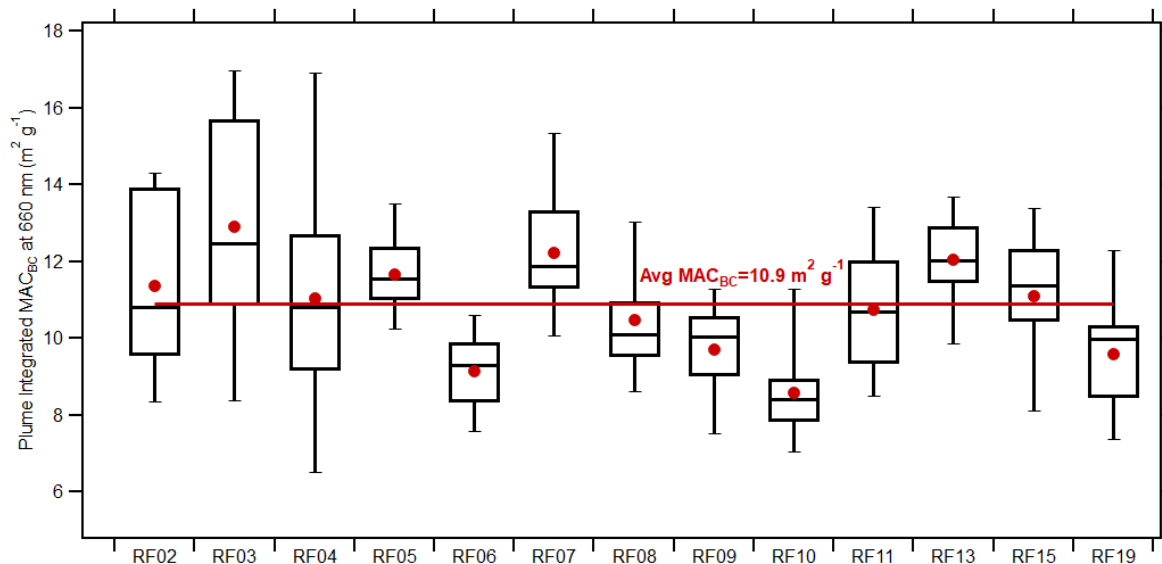


Figure 10: Box plots of plume integrated $\text{MAC}_{\text{BC660}}$ for each flight. On each box the central line represents the median, the top and bottom edges represent the 75th and 25th percentile, and the top and bottom whiskers represent the 90th and 10th percentile of the data. The red dot shows the average, and the red line indicates the average value for all plume integrated $\text{MAC}_{\text{BC660}}$.

571 MAC_{BC660} is also compared with the physical age and MCE (Fig. S13), the O:C and toluene:benzene chemical
572 clocks (Fig. S14), and the altitude, temperature and dilution (ΔCO) (Fig. S15). However, no clear trend is be found in
573 these comparisons.

574 The average absorption enhancement of 1.7 at 660 nm in this study indicates that, on average, 41% of total
575 absorption at 660 nm is caused by lensing and absorbing organics, instead of BC itself. Figure 11 shows the fraction
576 of non-BC absorption from BrC at 660 nm for the biomass burning plumes encountered during WE-CAN using Eq.
577 6-8 with OM calculated from the AMS. The figure is plotted versus plume physical age to allow visualization of the
578 variability, though there is no clear trend with physical age other than perhaps a decrease in variability with increasing
579 physical age. Figure S16 shows a similar result by using OM calculated from the UHSAS. More details on the
580 calculation and the AMS vs. UHSAS methods are explained in section 2.5. Assuming a MAC of the BC core of 6.3
581 $m^2 g^{-1}$, BrC contributes roughly the same amount of absorption at 660 nm as lensing (46% from the AMS method, 62%
582 from the UHSAS method). This means that 19% (AMS method) to 26% (UHSAS method) of the total absorption at
583 660 nm comes from BrC. When different particle density and WSOM:WSOC ratios are considered (top and bottom
584 whiskers, as well as red and blue dashed lines), the fraction of non-BC absorption is 41-49% for the AMS approach
585 (Fig. 11) and 43-80% for the UHSAS approach (Fig. S16) based on different OM:OC and density. The UHSAS
586 approach shows larger uncertainty because it's sensitive to the particle density when calculating particulate mass
587 (Table S1). While there is considerable variability between flights, a rule of thumb that roughly half of the non-BC
588 absorption at red wavelengths is from absorbing organic material seems reasonable. To the best of our knowledge, this
589 is the first observation-based attempt to differentiate between lensing and absorbing organics in the red wavelengths.
590 This approach assumes that water insoluble BrC has the same refractive index as water soluble BrC.

591

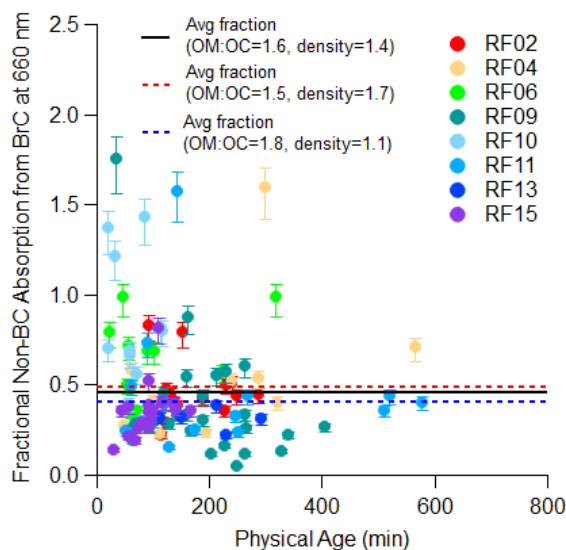


Figure 11: Time evolution of the fraction of non-BC absorption from BrC at 660 nm with AMS and Mie factor. Markers were calculated using a density of 1.4 g cm^{-3} and WSOM:WSOC ratio of 1.6. The top whiskers represent sensitive test values using a density of 1.7 g cm^{-3} and WSOM:WSOC ratio of 1.5, while the bottom whiskers represent sensitive test values using a density of 1.1 g cm^{-3} and WSOM:WSOC ratio of 1.8. The averaged fraction of non-BC absorption from BrC from all the plumes are shown in black solid lines, while the range of this result from sensitivity tests are shown in red and blue dashed lines.

592 4 Conclusion

593 In this study, we presented results that enable a better understanding of the ability of aerosol emissions from
 594 wildfires to absorb visible light and how those properties change after emission. We presented mass absorption
 595 coefficients (MAC) for BC and BrC from Western United States wildfires measured during the WE-CAN campaign
 596 at both short and long visible wavelengths ($\text{MAC}_{\text{BC}660}$, $\text{MAC}_{\text{BrC+lensing}_660}$, $\text{MAC}_{\text{ws}_\text{BrC}660}$, $\text{MAC}_{\text{BrC+lensing}_405}$). We also
 597 investigated the bulk absorption coefficient for BrC and bulk scattering coefficient for total aerosol at both short and
 598 long visible wavelengths. General trends that held for all the fire sources are derived, which should be valid throughout
 599 the western U.S. given the wide variety of emissions used to develop them.

600 By utilizing a common parameterization for BrC refractive index from Saleh et al. (2014), with measured
 601 inputs for the BC:OA ratio and particle size, we calculated the theoretical $\text{MAC}_{\text{BrC}660}$ and $\text{MAC}_{\text{BrC}405}$, and they were
 602 2.3~3.4 times larger than the measured $\text{MAC}_{\text{BrC+lensing}}$ during WE-CAN. While this discrepancy has been resolved
 603 previously by implementing bleaching into model schemes, we show that this is probably the incorrect explanation
 604 given the MAC of BrC either remains constant or slightly increases when chemical markers (O:C, toluene:benzene)
 605 suggest more oxidation has occurred. We suggest a different parameterization of the refractive index is needed to
 606 represent wildfire optical properties in the Western United States rather than using bleaching to decrease the mass
 607 absorption cross section (MAC) of the Saleh parameterization. We also note that there needs to be better terminology
 608 to distinguish between decreasing absorption caused by losses of organic aerosol mass versus decreasing absorption
 609 caused by changes in the MAC of the aerosol.

610 In the blue visible wavelengths, where BrC is more often thought about, $MAC_{BrC+lensing_405}$ is $0.59 \pm 0.19 \text{ m}^2$
611 g^{-1} and shows little variation with physical age, MCE, altitude, temperature or BC:OA ratio. There isn't any decreasing
612 trends in all the MAC_{BrC} data we obtained (MAC_{ws_BrC405} , $MAC_{BrC+lensing_405}$, MAC_{ws_BrC660} , and $MAC_{BrC+lensing_660}$)
613 with markers of chemical age (toluene:benzene, O:C), but bulk absorption of BrC does decrease with these same
614 markers. In highly aged plumes from multiple fires (RF05 and RF08), the $MAC_{BrC+lensing_405}$ has an average value of
615 $0.63 \pm 0.2 \text{ m}^2 \text{ g}^{-1}$, suggesting that brown carbon remains significantly absorbing even at relatively longer ages.

616 We find that total organic aerosol (OA) and water-soluble organic carbon (WSOC) are strongly correlated
617 with chemical markers of oxidative age. OA and WSOC (both normalized to CO) decrease with decreasing
618 toluene:benzene ratio and increasing O:C ratio. However, this phenomenon is only clearly observed when data from
619 all the observed fires is included rather than during the aging of individual fire plumes. This could mean that the fires
620 either had different emission ratios of toluene:benzene and O:C or the smoke underwent rapid secondary chemistry
621 prior to the first plume pass in WE-CAN. Regardless, the correlations are fairly robust (R^2 of 0.4 to 0.8) given the
622 many variables (MCE, fuel type, etc.) that are changing in the dataset and provide a potential link between chemical
623 markers and total organic aerosol amounts across a wide range of fires. While OA and WSOC decrease with decreasing
624 toluene:benzene or increasing O:C, MAC_{BrC} actually shows a weak increasing trend with these same markers of aging,
625 showing that while the total amount of organic aerosol is decreasing, the ability of the organic to absorb per mass is
626 staying relatively constant, or even increasing. We also found that the bulk scattering coefficient (normalized to CO)
627 decreases with decreasing toluene:benzene ratio or increasing O:C ratio due to less OA being present, which leads to
628 a very different net radiative effect than that which results from just changing the refractive index of BrC.

629 In the red visible wavelengths, where BrC is often less noticed, we observed that the MAC of BC stayed
630 relatively constant across all plumes measured and at all physical ages (ages up to 15 hours observed), with an averaged
631 MAC_{BC660} of $10.9 \pm 2.1 \text{ m}^2 \text{ g}^{-1}$ (average \pm standard deviation), which includes the contribution from both lensing effect
632 and absorbing organics. This average showed no clear trends with altitude or temperature, and we saw no evidence
633 that MAC_{BC660} is correlated to MCE. Even in highly aged plumes with emissions mixed from multiple fires (RF05
634 and RF08), the MAC_{BC660} is similar in magnitude to the near-source plumes with an average of $11.3 \pm 1.8 \text{ m}^2 \text{ g}^{-1}$. Both
635 the fact that this MAC is significantly larger than the MAC for uncoated BC (often cited to be $\sim 6.3 \text{ m}^2 \text{ g}^{-1}$) and the
636 fact that the MAC remains relatively constant across different fires and different plume ages are key insights that can
637 improve models of aerosol optical properties in wildfire emissions.

638 Through a novel use of PILS data, we find that BrC contributes 41-80% of non-BC absorption at 660 nm
639 (assuming $6.3 \text{ m}^2 \text{ g}^{-1}$ as the MAC of BC core at 660 nm). BrC contributes, on average, 26% of total absorption, but
640 the absorption cross section of water-soluble BrC is relatively small at 660 nm, with a MAC_{ws_BrC660} of $0.03 \pm 0.02 \text{ m}^2$
641 g^{-1} , which does not change with physical age, and no trend with MCE is observed. The average $MAC_{BrC+lensing_660}$
642 derived from the PAS (which includes both brown carbon absorption and lensing of black carbon) is $0.11 \pm 0.06 \text{ m}^2$
643 g^{-1} .

644 **Data Availability**

645 The WE-CAN data can be found at http://data.eol.ucar.edu/master_lists/generated/we-can/.

646 The DOI for each data set used in this work are:
647 PAS and CAPS PM_{SSA}: <https://doi.org/10.26023/K8P0-X4T3-TN06>
648 PILS1: <https://doi.org/10.26023/9H07-MD9K-430D> and <https://doi.org/10.26023/CRHY-NDT9-C30V>
649 PILS2: <https://doi.org/10.26023/7TAN-TZMD-680Y>
650 SP2: <https://doi.org/10.26023/P8R2-RAB6-N814>
651 UHSAS: <https://doi.org/10.26023/BZ4F-EAC4-290W>
652 PTR-ToF-MS: <https://doi.org/10.26023/K9F4-2CNH-EQ0W>
653 HR-AMS: <https://doi.org/10.26023/MM2Y-ZGFQ-RB0B>
654 Picarro: <https://doi.org/10.26023/NNYM-Z18J-PX0Q>
655 miniQCL: <https://doi.org/10.26023/Q888-WZRD-B70F>

656 **Author Contributions**

657 SMM designed the project. YS wrote the paper. YS, RPP, APS, EJTL, LAG, DKF, WP, LH, DWT, TC, EVF, and SMM
658 collected and analyzed data.

659 **Competing Interests**

660 The authors declare that they have no conflict of interest.

661 **Acknowledgements**

662 The 2018 WE-CAN field campaign was supported by the U.S. National Science Foundation through grants AGS-
663 1650493 (U of Wyoming), AGS-1650786 (Colorado State U), AGS-1650275 (U of Montana), AGS-1650288 (U of
664 Colorado at Boulder), and the National Oceanic and Atmospheric Administration (Award # NA17OAR4310010,
665 Colorado State U). This material is based upon study supported by the National Center for Atmospheric Research,
666 which is a major facility sponsored by the National Science Foundation under Cooperative Agreement no. 1852977.
667 The authors acknowledge support from AGS-1650493 for YS, SMM and RPP, AGS-1650786 for APS and EJTL,
668 AGS-2144896 for LH and WP, AGS-1650288 for DWT, NOAA Climate Program Office's Atmospheric Chemistry,
669 Carbon Cycle, and Climate program (Grant NA17OAR4310010) for DKF and LAG.

670

671 We sincerely thank Ernie Lewis for his work implementing Mie theory into Igor code.

672 **References**

673 Aiken, A. C., Decarlo, P. F., Kroll, J. H., Worsnop, D. R., Huffman, J. A., Docherty, K. S., et al. (2008). O/C and
674 OM/OC ratios of primary, secondary, and ambient organic aerosols with high-resolution time-of-flight aerosol

675 mass spectrometry. *Environmental Science and Technology*, 42(12), 4478–4485.
676 <https://doi.org/10.1021/es703009q>

677 Akagi, S. K., Yokelson, R. J., Wiedinmyer, C., Alvarado, M. J., Reid, J. S., Karl, T., et al. (2011). Emission factors
678 for open and domestic biomass burning for use in atmospheric models. *Atmospheric Chemistry and Physics*,
679 11(9), 4039–4072. <https://doi.org/10.5194/acp-11-4039-2011>

680 Andreae, M. O. (2019). Emission of trace gases and aerosols from biomass burning – An updated assessment.
681 *Atmospheric Chemistry and Physics Discussions*, 1–27. <https://doi.org/10.5194/acp-2019-303>

682 Andreae, M. O., & Gelencsér, A. (2006). Black carbon or brown carbon? The nature of light-absorbing carbonaceous
683 aerosols. *Atmospheric Chemistry and Physics*, 6, 3131–3148. <https://doi.org/10.5194/acp-6-3131-2006>

684 Bahadur, R., Praveen, P. S., Xu, Y., & Ramanathan, V. (2012). Solar absorption by elemental and brown carbon
685 determined from spectral observations. *Proceedings of the National Academy of Sciences*, 109(43), 17366–
686 17371. <https://doi.org/10.1073/pnas.1205910109>

687 Bohren, C. F., and Huffman, D. R. (1983). Absorption and Scattering of Light by Small Particles. John Wiley & Sons,
688 Inc.

689 Bond, T. C., & Bergstrom, R. W. (2006). Light absorption by carbonaceous particles: An investigative review. *Aerosol*
690 *Science and Technology*, 40(1), 27–67. <https://doi.org/10.1080/02786820500421521>

691 Bond, T. C., Habib, G., & Bergstrom, R. W. (2006). Limitations in the enhancement of visible light absorption due to
692 mixing state. *Journal of Geophysical Research Atmospheres*, 111(20), 1–13.
693 <https://doi.org/10.1029/2006JD007315>

694 Bond, T. C., Doherty, S. J., Fahey, D. W., Forster, P. M., Bernsten, T., Deangelo, B. J., et al. (2013). Bounding the
695 role of black carbon in the climate system: A scientific assessment. *Journal of Geophysical Research*
696 *Atmospheres*, 118(11), 5380–5552. <https://doi.org/10.1002/jgrd.50171>

697 Brown, H., Liu, X., Feng, Y., Jiang, Y., Wu, M., Lu, Z., et al. (2018). Radiative effect and climate impacts of brown
698 carbon with the Community Atmosphere Model (CAM5). *Atmospheric Chemistry and Physics*, 18(24), 17745–
699 17768. <https://doi.org/10.5194/acp-18-17745-2018>

700 Brown, H., Liu, X., Pokhrel, R., Murphy, S., Lu, Z., Saleh, R., et al. (2021). Biomass burning aerosols in most climate
701 models are too absorbing. *Nature Communications*, 12(1), 1–15. <https://doi.org/10.1038/s41467-020-20482-9>

702 Burke, M., Driscoll, A., Heft-Neal, S., Xue, J., Burney, J., & Wara, M. (2021). The changing risk and burden of
703 wildfire in the United States. *Proceedings of the National Academy of Sciences of the United States of America*,
704 118(2), 1–6. <https://doi.org/10.1073/PNAS.2011048118>

705 Canagaratna, M. R., Jimenez, J. L., Kroll, J. H., Chen, Q., Kessler, S. H., Massoli, P., et al. (2015). Elemental ratio
706 measurements of organic compounds using aerosol mass spectrometry : characterization , improved calibration ,
707 and implications. *Atmospheric Chemistry and Physics*, 15(1), 253–272. [https://doi.org/10.5194/acp-15-253-](https://doi.org/10.5194/acp-15-253-2015)
708 [2015](https://doi.org/10.5194/acp-15-253-2015)

709 Cappa, C. D., Onasch, T. B., Massoli, P., Worsnop, D. R., Bates, T. S., Cross, E. S., et al. (2012). Radiative absorption
710 enhancements due to the mixing state of atmospheric black carbon. *Science*, 337(6098), 1078–1081.
711 <https://doi.org/10.1126/science.1223447>

712 Cappa, C. D., Zhang, X., Russell, L. M., Collier, S., Lee, A. K. Y., Chen, C. L., et al. (2019). Light Absorption by
713 Ambient Black and Brown Carbon and its Dependence on Black Carbon Coating State for Two California, USA,
714 Cities in Winter and Summer. *Journal of Geophysical Research: Atmospheres*, 124(3), 1550–1577.
715 <https://doi.org/10.1029/2018JD029501>

716 Carter, T. S., Heald, C. L., Cappa, C. D., Kroll, J. H., Campos, T. L., Coe, H., et al. (2021). Investigating Carbonaceous
717 Aerosol and its Absorption Properties from Fires in the western US (WE-CAN) and southern Africa (ORACLES
718 and CLARIFY). *Journal of Geophysical Research Atmospheres*, 1–28. <https://doi.org/10.1029/2021JD034984>

719 Chen, M., Sun, Z., Davis, J. M., Liu, Y. A., Corr, C. A., & Gao, W. (2019). Improving the mean and uncertainty of
720 ultraviolet multi-filter rotating shadowband radiometer in situ calibration factors: Utilizing Gaussian process
721 regression with a new method to estimate dynamic input uncertainty. *Atmospheric Measurement Techniques*,
722 12(2), 935–953. <https://doi.org/10.5194/amt-12-935-2019>

723 Cho, C., Kim, S. W., Lee, M., Lim, S., Fang, W., Gustafsson, Ö., et al. (2019). Observation-based estimates of the
724 mass absorption cross-section of black and brown carbon and their contribution to aerosol light absorption in
725 East Asia. *Atmospheric Environment*, 212(November 2018), 65–74.
726 <https://doi.org/10.1016/j.atmosenv.2019.05.024>

727 Craig, L., Moharreri, A., Schanot, A., Rogers, D. C., Dhaniyala, S., Craig, L., et al. (2013a). Characterizations of
728 Cloud Droplet Shatter Artifacts in Two Airborne Aerosol Inlets. *Aerosol Science and Technology*, 47:6, 662–
729 671. <https://doi.org/10.1080/02786826.2013.780648>

730 Craig, L., Schanot, A., Moharreri, A., Rogers, D. C., & Dhaniyala, S. (2013b). Design and Sampling Characteristics
731 of a New Airborne Aerosol Inlet for Aerosol Measurements in Clouds. *Journal of Atmospheric and Oceanic
732 Technology*, 30, 1123–1135. <https://doi.org/10.1175/JTECH-D-12-00168.1>

733 Craig, L., Moharreri, A., Rogers, D. C., Anderson, B., & Dhaniyala, S. (2014). Aircraft-Based Aerosol Sampling in
734 Clouds : Performance Characterization of Flow-Restriction Aerosol Inlets. *Journal of Atmospheric and Oceanic
735 Technology*, 31, 2512–2521. <https://doi.org/10.1175/JTECH-D-14-00022.1>

736 Duarte, R. M. B. O., Freire, S. M. S. C., & Duarte, A. C. (2015). Investigating the water-soluble organic functionality
737 of urban aerosols using two-dimensional correlation of solid-state ¹³C NMR and FTIR spectral data.
738 *Atmospheric Environment*, 116, 245–252. <https://doi.org/10.1016/j.atmosenv.2015.06.043>

739 Duarte, R. M. B. O., Piñeiro-Iglesias, M., López-Mahía, P., Muniategui-Lorenzo, S., Moreda-Piñeiro, J., Silva, A. M.
740 S., & Duarte, A. C. (2019). Comparative study of atmospheric water-soluble organic aerosols composition in
741 contrasting suburban environments in the Iberian Peninsula Coast. *Science of the Total Environment*, 648, 430–
742 441. <https://doi.org/10.1016/j.scitotenv.2018.08.171>

743 Eatough, D. J., Wadsworth, A., Eatough, D. A., Crawford, J. W., Hansen, L. D., & Lewis, E. A. (1993). A multiple-
744 system, multi-channel diffusion denuder sampler for the determination of fine-particulate organic material in
745 the atmosphere. *Atmospheric Environment Part A, General Topics*, 27(8), 1213–1219.
746 [https://doi.org/10.1016/0960-1686\(93\)90247-V](https://doi.org/10.1016/0960-1686(93)90247-V)

747 Finessi, E., Decesari, S., Paglione, M., Giulianelli, L., Carbone, C., Gilardoni, S., et al. (2012). Determination of the
748 biogenic secondary organic aerosol fraction in the boreal forest by NMR spectroscopy. *Atmospheric Chemistry
749 and Physics*, 12(2), 941–959. <https://doi.org/10.5194/acp-12-941-2012>

750 Ford, B., Val Martin, M., Zelasky, S. E., Fischer, E. V., Anenberg, S. C., Heald, C. L., & Pierce, J. R. (2018). Future
751 Fire Impacts on Smoke Concentrations, Visibility, and Health in the Contiguous United States. *GeoHealth*, 2(8),
752 229–247. <https://doi.org/10.1029/2018gh000144>

753 Forrister, Haviland; Liu, Jiumeng; Scheuer, Eric; Dibb, Jack; Ziemba, Luke; Thornhill, L. Kenneth; Anderson, Bruce;
754 Diskin, Glenn; Perring, E. Anne; P. Schwarz, Joshua; Campuzano-Jost, Pedro; A. Day, Douglas; B. Palm, Brett;
755 Jimenez, L. Jose; Nenes, Athan, R. J. (2015). Evolution of brown carbon in wildfire plumes. *Geophysical
756 Research Letters*, 42, 4623–4630. <https://doi.org/10.1002/2015GL063897>

757 Foster, K., Pokhrel, R., Burkhart, M., & Murphy, S. (2019). A novel approach to calibrating a photoacoustic absorption
758 spectrometer using polydisperse absorbing aerosol. *Atmospheric Measurement Techniques*, 12(6), 3351–3363.
759 <https://doi.org/10.5194/amt-12-3351-2019>

760 Fuller, K. A., & Kreidenweis, S. M. (1999). Effects of mixing on extinction by carbonaceous particles. *Journal of
761 Geophysical Research*, 104(D13), 15941–15954. <https://doi.org/10.1029/1998JD100069>

762 Garofalo, L. A., Pothier, M. A., Levin, E. J. T., Campos, T., Kreidenweis, S. M., & Farmer, D. K. (2019). Emission
763 and Evolution of Submicron Organic Aerosol in Smoke from Wildfires in the Western United States. *ACS Earth
764 and Space Chemistry*, 3(7), 1237–1247. <https://doi.org/10.1021/acsearthspacechem.9b00125>

765 Grieshop, A. P., Logue, J. M., Donahue, N. M., & Robinson, A. L. (2009). Laboratory investigation of photochemical
766 oxidation of organic aerosol from wood fires 1: Measurement and simulation of organic aerosol evolution.
767 *Atmospheric Chemistry and Physics*, 9(4), 1263–1277. <https://doi.org/10.5194/acp-9-1263-2009>

768 Gouw, J. A. De, Middlebrook, A. M., Warneke, C., Goldan, P. D., Kuster, W. C., Roberts, J. M., et al. (2005). Budget
769 of organic carbon in a polluted atmosphere : Results from the New England Air Quality Study in 2002. *Journal
770 of Geophysical Research*, 110, 1–22. <https://doi.org/10.1029/2004JD005623>

771 Healy, R. M., Wang, J. M., Jeong, C. H., Lee, A. K. Y., Willis, M. D., Jaroudi, E., et al. (2015). Light-absorbing
772 properties of ambient black carbon and brown carbon from fossil fuel and biomass burning sources. *Journal of
773 Geophysical Research: Atmospheres*, 120(13), 6619–6633. <https://doi.org/10.1002/2015JD023382>

774 Hecobian, A., Zhang, X., Zheng, M., Frank, N., Edgerton, E. S., & Weber, R. J. (2010). Water-soluble organic aerosol
775 material and the light-absorption characteristics of aqueous extracts measured over the Southeastern United
776 States. *Atmospheric Chemistry and Physics*, 10(13), 5965–5977. <https://doi.org/10.5194/acp-10-5965-2010>

777 Hurteau, M. D., Westerling, A. L., Wiedinmyer, C., & Bryant, B. P. (2014). Projected effects of climate and
778 development on California wildfire emissions through 2100. *Environmental Science and Technology*, 48(4),
779 2298–2304. <https://doi.org/10.1021/es4050133>

780 Kirchstetter, T. W., Novakov, T., & Hobbs, P. V. (2004). Evidence that the spectral dependence of light absorption
781 by aerosols is affected by organic carbon. *Journal of Geophysical Research D: Atmospheres*, 109(21), 1–12.
782 <https://doi.org/10.1029/2004JD004999>

783 Krasowsky, T. S., McMeeking, G. R., Wang, D., Sioutas, C., & Ban-Weiss, G. A. (2016). Measurements of the impact
784 of atmospheric aging on physical and optical properties of ambient black carbon particles in Los Angeles.
785 *Atmospheric Environment*, 142, 496–504. <https://doi.org/10.1016/j.atmosenv.2016.08.010>

786 Kleinman, L. I., Sedlacek, A. J., Adachi, K., Buseck, P. R., Collier, S., Dubey, M. K., et al. (2020). Rapid evolution
787 of aerosol particles and their optical properties downwind of wildfires in the western US. *Atmospheric Chemistry
788 and Physics*, 20(21), 13319–13341. <https://doi.org/10.5194/acp-20-13319-2020>

789 Lack, D. A., Lovejoy, E. R., Baynard, T., Pettersson, A., & Ravishankara, A. R. (2006). Aerosol Absorption
790 Measurement using Photoacoustic Spectroscopy: Sensitivity, Calibration, and Uncertainty Developments.
791 *Aerosol Science and Technology*, 40(9), 697–708. <https://doi.org/10.1080/02786820600803917>

792 Lack, D. A., & Cappa, C. D. (2010). Impact of brown and clear carbon on light absorption enhancement, single scatter
793 albedo and absorption wavelength dependence of black carbon. *Atmospheric Chemistry and Physics*, 10(9),
794 4207–4220. <https://doi.org/10.5194/acp-10-4207-2010>

795 Lack, D. A., Langridge, J. M., Bahreini, R., Cappa, C. D., Middlebrook, A. M., & Schwarz, J. P. (2012a). Brown
796 carbon and internal mixing in biomass burning particles. *Proceedings of the National Academy of Sciences of
797 the United States of America*, 109(37), 14802–14807. <https://doi.org/10.1073/pnas.1206575109>

798 Lack, D. A., Richardson, M. S., Law, D., Langridge, J. M., Cappa, C. D., McLaughlin, R. J., & Murphy, D. M. (2012b).
799 Aircraft Instrument for Comprehensive Characterization of Aerosol Optical Properties, Part 2: Black and Brown
800 Carbon Absorption and Absorption Enhancement Measured with Photo Acoustic Spectroscopy. *Aerosol Science
801 and Technology*, 46(5), 555–568. <https://doi.org/10.1080/02786826.2011.645955>

802 Lindaas, J., Pollack, I. B., Garofalo, L. A., Pothier, M. A., Farmer, D. K., Kreidenweis, S. M., et al. (2021). Emissions
803 of Reactive Nitrogen From Western U.S. Wildfires During Summer 2018. *Journal of Geophysical Research:
804 Atmospheres*, 126(2), 1–21. <https://doi.org/10.1029/2020JD032657>

805 Liu, D., Whitehead, J., Alfara, M. R., Reyes-villegas, E., Spracklen, D. V., Reddington, C. L., et al. (2017). Black-
806 carbon absorption enhancement in the atmosphere determined by particle mixing state. *Nature Geoscience*,
807 10(3), 184–188. <https://doi.org/10.1038/NGEO2901>

808 Liu, D., He, C., Schwarz, J. P., & Wang, X. (2020). Lifecycle of light-absorbing carbonaceous aerosols in the
809 atmosphere. *Npj Climate and Atmospheric Science*, 3(40). <https://doi.org/10.1038/s41612-020-00145-8>

810 Liu, J., Bergin, M., Guo, H., King, L., Kotra, N., Edgerton, E., & Weber, R. J. (2013). Size-resolved measurements of
811 brown carbon in water and methanol extracts and estimates of their contribution to ambient fine-particle light
812 absorption. *Atmospheric Chemistry and Physics*, 13(24), 12389–12404. [https://doi.org/10.5194/acp-13-12389-
813 2013](https://doi.org/10.5194/acp-13-12389-2013)

814 Liu, S., Aiken, A. C., Gorkowski, K., Dubey, M. K., Cappa, C. D., Williams, L. R., et al. (2015). Enhanced light
815 absorption by mixed source black and brown carbon particles in UK winter. *Nature Communications*, 6, 8435.
816 <https://doi.org/10.1038/ncomms9435>

817 Marple, V. A., Rubow, K. L., & Behm, S. M. (1991). A microorifice uniform deposit impactor (moudi): Description,
818 calibration, and use. *Aerosol Science and Technology*, 14(4), 434–436.
819 <https://doi.org/10.1080/02786829108959504>

820 McClure, C. D., Lim, C. Y., Hagan, D. H., Kroll, J. H., & Cappa, C. D. (2020). Biomass-burning-derived particles
821 from a wide variety of fuels - Part 1: Properties of primary particles. *Atmospheric Chemistry and Physics*,
822 20(3), 1531–1547. <https://doi.org/10.5194/acp-20-1531-2020>

823 McConnell, J. R., Edwards, R., Kok, L. G., Flanner, M. G., Zender, C. S., Saltzman, E. S., et al. (2007). 20th-Century
824 Industrial Black Carbon Emissions Altered Arctic Climate Forcing. *Science*, 317(5843), 1381–1384.
825 <https://doi.org/10.1126/science.1144856>

826 Moharreri, A., Craig, L., Dubey, P., Rogers, D. C., & Dhaniyala, S. (2014). Aircraft testing of the new Blunt-body
827 Aerosol Sampler (BASE). *Atmospheric Measurement Techniques*, 7(9), 3085–3093.
828 <https://doi.org/10.5194/amt-7-3085-2014>

829 Neumann, J. E., Amend, M., Anenberg, S., Kinney, P. L., Sarofim, M., Martinich, J., et al. (2021). Estimating PM_{2.5}-
830 related premature mortality and morbidity associated with future wildfire emissions in the western US.
831 *Environmental Research Letters*, 16(3). <https://doi.org/10.1088/1748-9326/abe82b>

832 Onasch, T. B., Massoli, P., Keegan, P. L., Hills, F. B., Bacon, F. W., & Freedman, A. (2015). Single scattering
833 albedo monitor for airborne particulates. *Aerosol Science and Technology*, 49(4), 267–279.
834 <https://doi.org/10.1080/02786826.2015.1022248>

835 Orsini, D. A., Ma, Y., Sullivan, A., Sierau, B., Baumann, K., & Weber, R. J. (2003). Refinements to the particle-into-
836 liquid sampler (PILS) for ground and airborne measurements of water soluble aerosol composition. *Atmospheric*
837 *Environment*, 37(9–10), 1243–1259. [https://doi.org/10.1016/S1352-2310\(02\)01015-4](https://doi.org/10.1016/S1352-2310(02)01015-4)

838 Palm, B. B., Peng, Q., Fredrickson, C. D., Lee, B. H., Garofalo, L. A., Pothier, M. A., et al. (2020). Quantification of
839 organic aerosol and brown carbon evolution in fresh wildfire plumes. *Proceedings of the National Academy of*
840 *Sciences of the United States of America*, 117(47), 29469–29477. <https://doi.org/10.1073/pnas.2012218117>

841 Peltier, R. E., Weber, R. J., & Sullivan, A. P. (2007). Investigating a liquid-based method for online organic carbon
842 detection in atmospheric particles. *Aerosol Science and Technology*, 41(12), 1117–1127.
843 <https://doi.org/10.1080/02786820701777465>

844 Peng, J., Hu, M., Guo, S., Du, Z., Zheng, J., Shang, D., et al. (2016). Markedly enhanced absorption and direct radiative
845 forcing of black carbon under polluted urban environments. *Proceedings of the National Academy of Sciences*
846 *of the United States of America*, 113(16), 4266–4271. <https://doi.org/10.1073/pnas.1602310113>

847 Peng, Q., Palm, B. B., Melander, K. E., Lee, B. H., Hall, S. R., Ullmann, K., et al. (2020). HONO Emissions from
848 Western U.S. Wildfires Provide Dominant Radical Source in Fresh Wildfire Smoke. *Environmental Science and*
849 *Technology*, 54(10), 5954–5963. <https://doi.org/10.1021/acs.est.0c00126>

850 Permar, W., Wang, Q., Selimovic, V., Wielgasz, C., Yokelson, R. J., Hornbrook, R. S., et al. (2021). Emissions of
851 Trace Organic Gases From Western U.S. Wildfires Based on WE-CAN Aircraft Measurements. *Journal of*
852 *Geophysical Research: Atmospheres*, 126(11). <https://doi.org/10.1029/2020JD033838>

853 Pokhrel, R. P., Wagner, N. L., Langridge, J. M., Lack, D. A., Jayathne, T., Stone, E. A., et al. (2016).
854 Parameterization of single-scattering albedo (SSA) and absorption Ångström exponent (AAE) with EC/OC for
855 aerosol emissions from biomass burning. *Atmospheric Chemistry and Physics*, 16(15), 9549–9561.
856 <https://doi.org/10.5194/acp-16-9549-2016>

857 Pokhrel, R. P., Beamesderfer, E. R., Wagner, N. L., Langridge, J. M., Lack, D. A., Jayarathne, T., et al. (2017).
858 Relative importance of black carbon, brown carbon, and absorption enhancement from clear coatings in
859 biomass burning emissions. *Atmospheric Chemistry and Physics*, 17(8), 5063–5078.
860 <https://doi.org/10.5194/acp-17-5063-2017>

861 Rosencwaig, A. (1980). *Photoacoustics and photoacoustic spectroscopy*. *Annual Review of Biophysics and*
862 *Bioengineering*, 9, 31–54. <https://doi.org/10.1146/annurev.bb.09.060180.000335>

863 Saleh, R., Robinson, E. S., Tkacik, D. S., Ahern, A. T., Liu, S., Aiken, A. C., et al. (2014). Brownness of organics in
864 aerosols from biomass burning linked to their black carbon content. *Nature Geoscience*, 7(9), 647–650.
865 <https://doi.org/10.1038/ngeo2220>

866 Saleh, R. (2020). From Measurements to Models: Toward Accurate Representation of Brown Carbon in Climate
867 Calculations. *Current Pollution Reports*, 6(2), 90–104. <https://doi.org/10.1007/s40726-020-00139-3>

868 Sarangi, C., Qian, Y., Rittger, K., Leung, R. L., Chand, D., Bormann, K. J., & Painter, T. H. (2020). Dust dominates
869 high-altitude snow darkening and melt over high-mountain Asia. *Nature Climate Change*, (October), 1–7.
870 <https://doi.org/10.1038/s41558-020-00909-3>

871 Schnaiter, M., Horvath, H., Möhler, O., Naumann, K. H., Saathoff, H., & Schöck, O. W. (2003). UV-VIS-NIR spectral
872 optical properties of soot and soot-containing aerosols. *Journal of Aerosol Science*, 34(10), 1421–1444.
873 [https://doi.org/10.1016/S0021-8502\(03\)00361-6](https://doi.org/10.1016/S0021-8502(03)00361-6)

874 Schnaiter, M., Linke, C., Möhler, O., Naumann, K. H., Saathoff, H., Wagner, R., et al. (2005). Absorption
875 amplification of black carbon internally mixed with secondary organic aerosol. *Journal of Geophysical Research*
876 *D: Atmospheres*, 110(19), 1–11. <https://doi.org/10.1029/2005JD006046>

877 Schwarz, J. P., Gao, R. S., Fahey, D. W., Thomson, D. S., Watts, L. A., Wilson, J. C., et al. (2006). Single-particle
878 measurements of midlatitude black carbon and light-scattering aerosols from the boundary layer to the lower
879 stratosphere. *Journal of Geophysical Research*, 111, D16207. <https://doi.org/10.1029/2006JD007076>

880 Subramanian, R., Kok, G. L., Baumgardner, D., Clarke, A., Shinozuka, Y., Campos, T. L., et al. (2010). Black carbon
881 over Mexico: The effect of atmospheric transport on mixing state, mass absorption cross-section, and BC/CO
882 ratios. *Atmospheric Chemistry and Physics*, 10(1), 219–237. <https://doi.org/10.5194/acp-10-219-2010>

883 Sullivan, A. P., Pokhrel, R. P., Shen, Y., Murphy, S. M., Toohey, D. W., Campos, T., Lindaas, J., Fischer, E. V., and
884 Collett Jr., J. L. (2022). Examination of Brown Carbon Absorption from Wildfires in the Western U.S. During
885 the WE-CAN Study. *Atmospheric Chemistry and Physics*, 22(20), 13389–13406. <https://doi.org/10.5194/acp-22-13389-2022>

886

887 Sun, Y., Zhang, Q., Zheng, M., Ding, X., Edgerton, E. S., & Wang, X. (2011). Characterization and source
888 apportionment of water-soluble organic matter in atmospheric fine particles (PM_{2.5}) with high-resolution
889 aerosol mass spectrometry and GC-MS. *Environmental Science and Technology*, 45(11), 4854–4861.
890 <https://doi.org/10.1021/es200162h>

891 Szopa, S., V. Naik, B. Adhikary, P. Artaxo, T. Berntsen, W.D. Collins, S. et al. (2021): Short-Lived Climate Forcers.
892 In *Climate Change 2021: The Physical Science Basis*. Contribution of Working Group I to the Sixth Assessment

893 Report of the Intergovernmental Panel on Climate Change. Cambridge University Press, Cambridge, United
894 Kingdom and New York, NY, USA, pp. 817–922, <https://doi:10.1017/9781009157896.008>

895 Tasoglou, A., Louvaris, E., Florou, K., Liangou, A., Karnezi, E., Kaltsonoudis, C., et al. (2020). Aerosol light
896 absorption and the role of extremely low volatility organic compounds. *Atmospheric Chemistry and Physics*,
897 20(19), 11625–11637. <https://doi.org/10.5194/acp-20-11625-2020>

898 Taylor, J. W., Wu, H., Szpek, K., Bower, K., Crawford, I., Flynn, M. J., et al. (2020). Absorption closure in highly
899 aged biomass burning smoke. *Atmospheric Chemistry and Physics*, 20(19), 11201–11221.
900 <https://doi.org/10.5194/acp-20-11201-2020>

901 Wang, X., Sedlacek, A. J., DeSá, S. S., Martin, S. T., Alexander, M. L., Alexander, M. L., et al. (2016). Deriving
902 brown carbon from multiwavelength absorption measurements: Method and application to AERONET and
903 Aethalometer observations. *Atmospheric Chemistry and Physics*, 16(19), 12733–12752.
904 <https://doi.org/10.5194/acp-16-12733-2016>

905 Wang, X., Heald, C. L., Liu, J., Weber, R. J., Campuzano-Jost, P., Jimenez, J. L., et al. (2018). Exploring the
906 observational constraints on the simulation of brown carbon. *Atmospheric Chemistry and Physics*, 18(2), 635–
907 653. <https://doi.org/10.5194/acp-18-635-2018>

908 Wei, Y., Ma, L., Cao, T., Zhang, Q., Wu, J., Buseck, P. R., & Thompson, J. E. (2013). Light scattering and extinction
909 measurements combined with laser-induced incandescence for the real-time determination of soot mass
910 absorption cross section. *Analytical Chemistry*, 85(19), 9181–9188. <https://doi.org/10.1021/ac401901b>

911 Westerling, A. L., Hidalgo, H. G., Cayan, D. R., & Swetnam, T. W. (2006). Warming and Earlier Spring Increase
912 Western U. S. Forest Wildfire Activity. *Science*, 313(5789), 940–943. <https://doi.org/10.1126/science.1128834>

913 Williams, E. L., & Grosjean, D. (1990). Removal of Atmospheric Oxidants with Annular Denuders. *Environmental*
914 *Science and Technology*, 24(6), 811–814. <https://doi.org/10.1021/es00076a002>

915 Wonaschütz, A., Hittenberger, R., Bauer, H., Pournesmaeil, P., Klatzer, B., Caseiro, A., & Puxbaum, H. (2009).
916 Application of the integrating sphere method to separate the contributions of brown and black carbon in
917 atmospheric aerosols. *Environmental Science and Technology*, 43(4), 1141–1146.
918 <https://doi.org/10.1021/es8008503>

919 Yue, X., Mickley, L. J., Logan, J. A., & Kaplan, J. O. (2013). Ensemble projections of wildfire activity and
920 carbonaceous aerosol concentrations over the western United States in the mid-21st century. *Atmospheric*
921 *Environment*, 77, 767–780. <https://doi.org/10.1016/j.atmosenv.2013.06.003>

922 Zeng, L., Zhang, A., Wang, Y., Wagner, N. L., Katich, J. M., Schwarz, J. P., et al. (2020). Global Measurements of
923 Brown Carbon and Estimated Direct Radiative Effects. *Geophysical Research Letters*, 47(13).
924 <https://doi.org/10.1029/2020GL088747>

925 Zeng, L., Sullivan, A. P., Washenfelder, R. A., Dibb, J., Scheuer, E., Campos, T. L., et al. (2021). Assessment of
926 online water-soluble brown carbon measuring systems for aircraft sampling. *Atmospheric Measurement*
927 *Techniques*, 14(10), 6357–6378. <https://doi.org/10.5194/amt-14-6357-2021>

928 Zeng, L., Dibb, J., Scheuer, E., Katich, J. M., Schwarz, J. P., Bourgeois, I., et al. (2022). Characteristics and Evolution
929 of Brown Carbon in Western United States Wildfires. *Atmospheric Chemistry and Physics*, 22, 8009–8036.
930 <https://doi.org/10.5194/acp-22-8009-2022>

931 Zhang, L., Segal-Rozenhaimer, M., Che, H., Dang, C., Sedlacek III, A. J., Lewis, E. R., Dobracki, A., Wong, J. P. S.,
932 Formenti, P., Howell, S. G., and Nenes, A.: Light Absorption by Brown Carbon over the South-East Atlantic
933 Ocean, *Atmos. Chem. Phys. Discuss.* [preprint], <https://doi.org/10.5194/acp-2021-1000>, in review, 2022.

934 Zhang, Y., Forrister, H., Liu, J., Dibb, J., Anderson, B., Schwarz, J. P., et al. (2017). Top-of-atmosphere radiative
935 forcing affected by brown carbon in the upper troposphere. *Nature Geoscience*, 10(7), 486–489.
936 <https://doi.org/10.1038/ngeo2960>